

44 NEW & KNOWN M DWARF MULTIPLES IN THE SDSS-III/APOGEE M DWARF ANCILLARY SCIENCE SAMPLE

JACOB SKINNER,¹ KEVIN R. COVEY,² CHAD F. BENDER,³ NOAH RIVERA,³ NATHAN DE LEE,^{4,5} DIOGO SOUTO,⁶
DREW CHOJNOWSKI,⁷ NICHOLAS TROUP,⁸ CARLES BADENES,⁹ DMITRY BIZYAEV,⁷ CULLEN H. BLAKE,¹⁰
ADAM BURGASSER,¹¹ CALEB CAÑAS,¹² JOLEEN CARLBERG,¹³ YILEN GÓMEZ MAQUEO CHEW,¹⁴ ROHIT DESHPANDE,¹²
SCOTT W. FLEMING,¹³ J. G. FERNÁNDEZ-TRINCADO,^{15,16} D. A. GARCÍA-HERNÁNDEZ,^{17,18} FRED HEARTY,¹²
MARINA KOUNKEL,² PENÉLOPE LONGA-PEÑE,¹⁹ SUVRATH MAHADEVAN,¹² STEVEN R. MAJEWSKI,²⁰ DANTE MINNITI,²¹
DAVID NIDEVER,²² AUDREY ORAVETZ,⁷ KAIKE PAN,⁷ KEIVAN STASSUN,²³ RYAN TERRIEN,²⁴ AND OLGA ZAMORA^{17,18}

¹Department of Physics & Astronomy, Western Washington University, Bellingham, WA 98225, USA

²Dept. of Physics & Astronomy, Western Washington University, Bellingham, WA 98225, USA

³Department of Astronomy and Steward Observatory, University of Arizona, Tucson, AZ 85721, USA

⁴Department of Physics, Geology, and Engineering Technology, Northern Kentucky University, Highland Heights, KY 41099, USA

⁵Department of Physics & Astronomy, Vanderbilt University, Nashville, TN 37235, USA

⁶Observatório Nacional, Rua General José Cristino, 77, 20921-400 São Cristóvão, Rio de Janeiro, RJ, Brazil

⁷Apache Point Observatory and New Mexico State University, P.O. Box 59, Sunspot, NM 88349-0059, USA

⁸Department of Physics, Salisbury University, 1101 Camden Ave, Salisbury, MD 21801, USA

⁹Department of Physics and Astronomy, University of Pittsburgh, Allen Hall, 3941 O'Hara St, Pittsburgh PA 15260, USA

¹⁰Department of Physics and Astronomy, University of Pennsylvania, 209 South 33rd Street, Philadelphia, PA 19104, USA

¹¹Center for Astrophysics and Space Science, University of California San Diego, La Jolla, CA 92093, USA

¹²Department of Astronomy & Astrophysics, Pennsylvania State, 525 Davey Lab, University Park, PA 16802, USA

¹³Space Telescope Science Institute, Baltimore, MD, 21218, USA

¹⁴Instituto de Astronomía, Universidad Nacional Autónoma de México, Ciudad Universitaria, Ciudad de México, 04510, México

¹⁵Departamento de Astronomía, Casilla 160-C, Universidad de Concepción, Concepción, Chile

¹⁶Institut Utinam, CNRS UMR6213, Univ. Bourgogne Franche-Comté, OSU THETA, Observatoire de Besançon, BP 1615, 25010 Besançon Cedex, France

¹⁷Instituto de Astrofísica de Canarias (IAC), Vía Lactea s/n, E-38205 La Laguna, Tenerife, Spain

¹⁸Departamento de Astrofísica, Universidad de La Laguna (ULL), E-38206 La Laguna, Tenerife, Spain

¹⁹Unidad de Astronomía, Facultad de Ciencias Básicas, Avenida Angamos 601, Antofagasta 1270300, Chile

²⁰Department of Astronomy, University of Virginia, Charlottesville, VA 22904-4325, USA

²¹Pontificia Universidad Católica de Chile, Instituto de Astrofísica, Av. Vicuña Mackenna 4860, 782-0436 Macul, Santiago, Chile

²²Department of Physics, Montana State University, Bozeman, MT 59717, USA

²³Department of Physics and Astronomy, Vanderbilt University, VU Station 1807, Nashville, TN 37235, USA

²⁴Department of Physics & Astronomy, Carleton College, Northfield MN, 55057, USA

ABSTRACT

Binary stars make up a significant portion of all stellar systems. Consequently, an understanding of the bulk properties of binary stars is necessary for a full picture of star formation. Binary surveys indicate that both multiplicity fraction and typical orbital separation increase as functions of primary mass. Correlations with higher order architectural parameters such as mass ratio are less well constrained. We seek to identify and characterize double-lined spectroscopic binaries (SB2s) among the 1350 M dwarf ancillary science targets with APOGEE spectra in the SDSS-III

skinnej3@wwu.edu

kevin.covey@wwu.edu

cbender@email.arizona.edu

Data Release 13. We measure the degree of asymmetry in the APOGEE pipeline cross-correlation functions (CCFs), and use those metrics to identify a sample of 44 high-likelihood candidate SB2s. At least 11 of these SB2s are known, having been previously identified by Deshpande et al, and/or El Badry et al. We are able to extract radial velocities (RVs) for the components of 36 of these systems from their CCFs. With these RVs, we measure mass ratios for 29 SB2s and 5 SB3s. We use Bayesian techniques to fit maximum likelihood (but still preliminary) orbits for 4 SB2s with 8 or more distinct APOGEE observations. The observed (but incomplete) mass ratio distribution of this sample rises quickly towards unity. Two-sided Kolmogorov-Smirnov tests find probabilities of 18.3% and 18.7%, demonstrating that the mass ratio distribution of our sample is consistent with those measured by Pourbaix et al. and Fernandez et al., respectively.

Keywords: binaries: close - binaries: general - binaries: spectroscopic - stars: formation - stars: low-mass

1. INTRODUCTION

Models of stellar formation and evolution make predictions about the distribution and frequency of stellar binaries. Fragmentation of a protostellar core or circumstellar disk can produce the requisite pair of pre-main sequence stars (e.g., [Offner et al. 2010](#)), but only at much larger separations ($\sim 100\text{-}1000+$ AU; [Tohline 2002](#); [Kratler 2011](#)) than those that characterize close¹ binaries. Dynamical processes presumably drive some of these wider binaries into a close configuration, but the nature and timescale of this evolution remains unclear: mechanisms that may play a role include dynamical friction from gas in the surrounding disk or core (e.g., [Gorti & Bhatt 1996](#)), gravitational interactions in/dynamical decay of few-body systems (e.g., [Reipurth & Clarke 2001](#); [Bate et al. 2002](#)), Kozai oscillations ([Fabrycky & Tremaine 2007](#)) and/or tidal friction (e.g., [Kiseleva et al. 1998](#)).

Empirical study has provided some data with which to test these models. The multiplicity fraction (MF, $\frac{\# \text{multiples}}{\text{all stars}}$) is known to be an increasing function of primary mass: the lowest multiplicity rates are observed for substellar systems (MF $11^{+7}_{-2}\%$ implying a companion fraction (CF) $\frac{\# \text{stars with companions}}{\text{all stars}}$ of $\approx 20\%$; [Burgasser et al. \(2006\)](#)), and rise into the M dwarf regime, where the seminal measurement of the companion fraction over all separations remains that of [Fischer & Marcy \(1992\)](#): $42\% \pm 9\%$ for separations of $0.04\text{-}10^4$ AU. Yet larger multiplicity rates are found for stars of G-type ($46\% \pm 2\%$; [Raghavan et al. \(2010\)](#)) and F-type and earlier ($100\% \pm 20\%$; [Duchêne & Kraus \(2013\)](#)). There is also mounting evidence of a trend of binary separation increasing with primary mass ([Ward-Duong et al. 2015](#)). When corrected for incompleteness, the mass ratio distribution of close binaries is mostly flat ([Moe & Di Stefano 2017](#)).

M dwarfs are a particularly common result of the star formation process, and by virtue of their low masses, provide leverage for probing the link between primary mass, companion fraction, and orbital separation. Since the survey of [Fischer & Marcy \(1992\)](#), additional M dwarf multiplicity surveys have been conducted by [Clark et al. \(2012\)](#), [Shan et al. \(2015\)](#) and [Ward-Duong et al. \(2015\)](#), who used various observational techniques to identify 22, 12 and 65 multiple systems within samples of 1452, 150, and 245 M dwarfs, respectively. These measurements are consistent with the [Fischer & Marcy \(1992\)](#) result, suggesting a CF of 26-35% for separations

outside a key gap in coverage from 0.4-3 AU. The near-infrared spectra of the APOGEE survey are well suited to detect the faint, cool companions of M dwarfs. This gives us a window into the dynamic evolution of early systems, as well as developed systems in the low period regime. A survey of M dwarf double-lined spectroscopic binaries (SB2s) in clusters and the field could detect changes in the close binary fraction with age, providing a valuable clue as to whether low period binaries most often mutually form up close, or evolve through 3 body dynamics with a 3rd, distant companion.

In this paper, we search the APOGEE spectroscopic database for close, double-lined spectroscopic binaries with low-mass, M dwarf primaries. We utilize a classic approach, searching for sources whose spectra include two or more sets of photospheric absorption lines, with a clear radial velocity offset in at least one APOGEE observation. This approach compliments the recent search conducted by [El-Badry et al. \(2018b\)](#), using the direct spectral modeling approach validated by [El-Badry et al. \(2018a\)](#). The search completed by [El-Badry et al. \(2018b\)](#) is sensitive to multiple systems over a much larger range of orbital separations, as their method can detect spectral superpositions even with no radial velocity offset. While their search is sensitive to a much broader range of parameter space in the dimension of orbital separation, their spectral modeling approach is limited to stars with $T_{\text{eff}} > 4000$ K, providing motivation for a directed search for close, low-mass spectroscopic binaries.

We begin by introducing the observational data and describe our sample selection in §2. We describe our data analysis procedure, mass ratio measurements, and mass ratio distribution in §3. Section §4 contains the description of our orbit fitting procedure and results for 4 targets. Finally, we present our results in §5 and summarize our conclusions in §6. Appendix A contains notes on a mass estimation calculation mentioned in §4.2.

2. OBSERVATIONS AND SAMPLE SELECTION

2.1. SDSS-III APOGEE M dwarf Ancillary Targets

The SDSS-III ([Eisenstein et al. 2011](#)) APOGEE M dwarf Ancillary Program ([Deshpande et al. 2013](#); [Holtzman et al. 2015](#)) was designed to produce a large, homogeneous spectral library and kinematic catalog of nearby low-mass stars; these data products are useful for investigations of stellar astrophysics (e.g. [Souto et al. 2017](#); [Gilhool et al. 2018](#)), and for refining targeting procedures for current and future exoplanet search programs. These science goals are uniquely enabled by the APOGEE spectrograph ([Wilson et al. 2010, 2012](#)), which acquires high resolution ($R \sim 22,000$) near-infrared

¹ with separations on the order of 1AU. i.e. Non-interacting and spectroscopic.

spectra from each of 300 optical fibers. As deployed at the 2.5 meter SDSS telescope (Gunn et al. 2006), the APOGEE spectrograph achieves a field-of-view with a diameter of 3 degrees, making it a highly efficient instrument for surveying the stellar parameters of the constituents of Galactic stellar populations (Majewski et al. 2017). The SDSS DR13 data release (Albaret et al. 2017) includes 7152 APOGEE spectra of 1350 stars targeted by this ancillary program. Methods used to select targets for the SDSS ancillary program are described in full by Deshpande et al. (2013) and Zasowski et al. (2013); briefly, the targets were selected with one of the following methods:

- stars of spectral type M4 or later, typically toward the fainter end of APOGEE’s sensitivity range ($H \gtrsim 10$), were targeted by applying a set of magnitude ($7 < H < 12$) and color ($V - K_s > 5.0$; $0.4 < J - H < 0.65$; $0.1 < H - K_s < 0.42$) cuts to the catalog of northern high proper motion ($\mu > 150 \text{ mas yr}^{-1}$) stars assembled by Lépine & Shara (2005).
- M dwarfs of all spectral sub-classes, typically toward the brighter end of APOGEE’s sensitivity range ($H \lesssim 10$), were identified by applying simple spatial ($\text{DEC} > 0$) and magnitude ($H > 7$) cuts to the all-sky catalog of bright M dwarfs assembled by Lépine & Gaidos (2011).
- calibrators with precise, stable radial velocities (as measured by the California Planet Search team), reliable measurements of rotation velocity (Jenkins et al. 2009, $v \sin i$), active M dwarfs in the Kepler field (Ciardi et al. 2011; Walkowicz et al. 2011), or targets in the input catalog of the MEarth Project (Nutzman & Charbonneau 2008) were individually added to the sample.

Figure 1 shows the location of these 1350 ancillary targets in $J - H$ vs. $H - K_s$ color-color space, along with the full DR13 sample shown for context. Figure 2 compares the number of APOGEE observations obtained for objects identified here as binaries, relative to the number of observations obtained for the full DR13 sample and the subset of M dwarf ancillary science targets. On average, sources identified as SB2s have one more APOGEE observation than the median for the M dwarf ancillary science sample, reflecting the advantage that multi-epoch observations provide for identifying RV variable sources.

2.2. Identification as SB2s

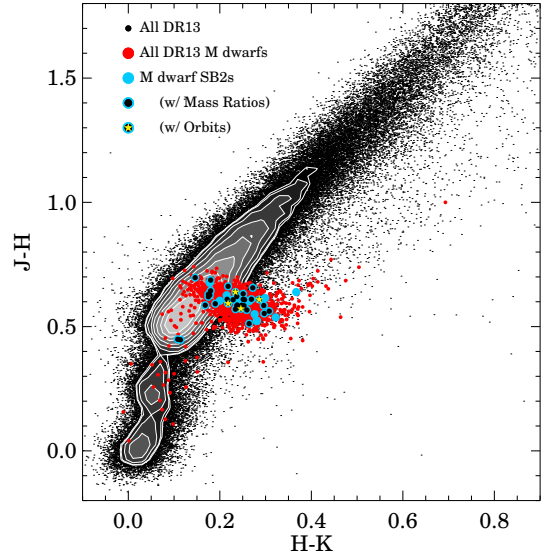


Figure 1. $J - H$ vs. $H - K_s$ color-color diagram of DR13 APOGEE targets. The full DR13 sample is shown as small points, and grayscale contours in areas of color-space where individual points can no longer be distinguished. M dwarf ancillary targets are shown as solid red dots, demonstrating the clear divergence from the reddened giant branch which makes up the bulk of the APOGEE dataset. Candidate SB2s are indicated with cyan dots; sources for which we infer mass ratios and full orbital fits are highlighted with a black central dot and surrounding ring, respectively.

Candidate SB2s were identified with an approach similar to that of Fernandez et al. (2017) (F17), who flagged sources with significant asymmetries in the cross-correlation functions (CCFs) calculated by the APOGEE pipeline (Nidever et al. 2015; García Pérez et al. 2016; Grieves et al. 2017). Following Fernandez et al. (2017), we characterized the asymmetry in each CCF using the R parameter originally developed by Tonry & Davis (1979):

$$R = \frac{H}{\sqrt{2}\sigma_a}$$

where H is the maximum of the CCF, and σ_a is the RMS of the anti-symmetric portion of the CCF. In this formalism, lower R values indicate sources with larger asymmetries in their CCF functions. To better identify sources with CCF asymmetries at physically meaningful velocity separations, we computed distinct R values for windows of differing widths around each CCF’s central peak. Specifically, we computed R values for the central 51, 101, and 151 lags in each CCF, which we denote as R_{51} , R_{101} , and R_{151} , respectively. Given the 4.14 km s^{-1} pixel spacing of the APOGEE spectra, these CCF windows provide sensitivity to secondaries with velocity

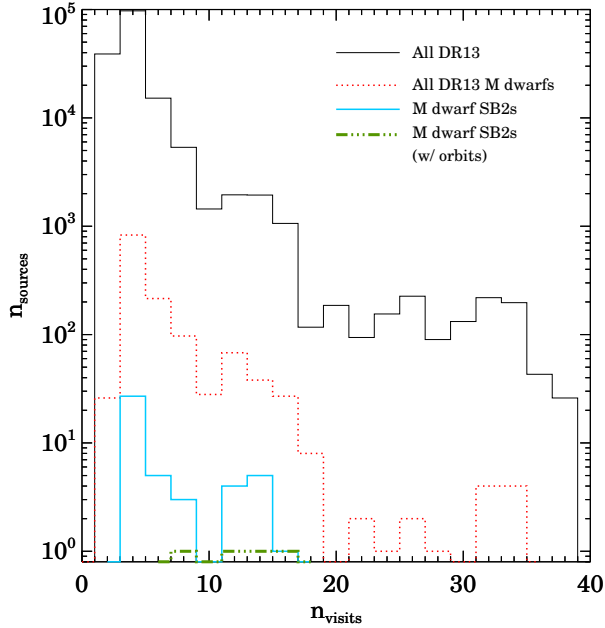


Figure 2. Histograms of the number of visits observed for different classes of APOGEE DR13 targets. The APOGEE M dwarf sample exhibits the same overall distribution of visits as the rest of the survey targets; the M dwarf SB2 candidates are modestly biased towards a larger number of visits, with ~ 1 more visit per system in both the median and the mean than the broader DR13 sample.

separations from the primary star of 106, 212, and 318 km s^{-1} .

We used a combination of absolute and relative criteria to identify candidate SB2s based on the lowest R values they exhibited across all their APOGEE observations. Selecting candidates on the basis of their lowest observed R values allows us to identify systems even if they only exhibit a clear velocity separation in a single epoch of APOGEE spectra. Absolute criteria ensure that each star’s CCF exhibits an asymmetry substantial enough to indicate the presence of a secondary star, while relative criteria based on ratios of the R values measured from different portions of the CCF (e.g., R_{51} , R_{151} , etc.) eliminate false positives due to sources whose CCFs exhibit significant asymmetries, but at velocities too large to be physically plausible for a bona fide SB2. We denote the smallest R value observed within a given CCF window across all a star’s APOGEE observations as \min_{R_W} (where W indicates the width of the CCF window the R value was computed from, such that $\min_{R_{151}}$ indicates the smallest R_{151} observed for a given star). To provide additional measures of the structure of each CCF, we also record the maximum response and bisector width of each CCF as *peak* and *bisector_x*, respectively.

Following the notation for the minimum R values across all epochs, we denote the maximum CCF response and bisector width across all observations as $\max_{bisector_x}$ and \max_{peak} , respectively. Using these measures of the structure detected across all CCFs computed for a given source, we identify candidate SB2s with the following criteria:

- To identify sources that exhibit a strong, central asymmetry on at least one epoch, we require:
 - $-\log_{10}(\min_{R_{101}}) < 0.83$
 - AND
 - $0.06 < \log_{10} \frac{\min_{R_{151}}}{\min_{R_{101}}} < 0.13$
 - OR
 - $-\log_{10}(\min_{R_{51}}) < 0.83$
 - AND
 - $0.05 < \log_{10} \frac{\min_{R_{101}}}{\min_{R_{51}}} < 0.2$
- To eliminate sources with weak CCF responses, suggesting a poor template match, we require:
 - $-\log_{10}(\max_{peak}) > -0.5$
- To eliminate sources whose CCF peaks are indicative of very low S/N or a reduction issue (i.e., too narrow or wide to be consistent with a single star or binary, or containing a greater degree of asymmetry than expected for 2-3 well detected CCF peaks), we require:

- $-0.7 > \log_{10}(\max_{bisector_x}) > 2.3$
- $-\log_{10}(\min_{R_{51}}) > 0.25$
- $-\log_{10}(\min_{R_{101}}) > 0.22$

These criteria identify 44 candidate M dwarf SB2s, or just more than 3% of all 1350 M dwarf ancillary targets in the DR13 catalog. These targets are listed in Table 1. Eight of these targets are among the 9 SB2s flagged by [Deshpande et al. \(2013\)](#) in their analysis of a subset of this sample, indicating that our methods are capable of recovering the majority of the short period, high flux ratio SB2s in the APOGEE database. The exception is 2MJ19333940+3931372, for which the APOGEE CCFs show evidence for profile changes, but the secondary component does not cleanly separate from the primary peak in any of the three visits obtained by APOGEE. Modifying our selection criteria to capture this source as a candidate SB2 would significantly increase the number of false positives that would need to be removed from our sample via visual inspection, so we choose to retain our more conservative cuts that will produce a smaller, but higher fidelity, sample of candidate SB2s.

2.3. Photometric Mass Estimates for Primary stars

We estimate the mass of the primary of each system in our sample using photometry and photometric calibrations from the literature. Photometric mass estimates are valuable for multiple reasons: the presence of multiple components in the system’s spectra renders the standard APOGEE/ASPCAP analysis unreliable, and the DR13 APOGEE parameters have been shown to be unreliable for even single M dwarfs (see [Souto et al. 2017](#)). For this photometric analysis, we adopted magnitudes from catalogs such as NOMAD ([Zacharias et al. 2005](#)), APOP ([Qi et al. 2015](#)), UCAC4 ([Zacharias et al. 2013](#)), UCAC5 ([Zacharias et al. 2017](#)), [Viaux et al. \(2013\)](#), and [Lépine & Shara \(2005\)](#). We did not attempt to infer or correct for stellar reddening in this process, as any extinction is expected to be minimal due to the stars’ presence within the solar neighborhood.

Stellar masses were derived using the ($V-K_s$) vs. mass color calibration derived by [Delfosse et al. \(2000\)](#). For stars without a reliable V magnitude reported in the literature, we adopted the M_K absolute magnitude vs. mass calibration derived by [Mann et al. \(2015\)](#). The absolute magnitudes were derived using distances in the literature. For the stars without distances reported we adopted $d = 20.0$ pc. The precision in the [Delfosse et al. \(2000\)](#) calibration is about 10%, which returns an uncertainty of $\sim \pm 0.05 M(M_\odot)$.

2.4. Additional RV monitoring with HET/HRS

We supplemented the APOGEE observations for a few systems with visible light spectroscopy from the fiber-fed High Resolution Spectrograph (hereafter, HRS; [Tull \(1998\)](#)) on the 9.2 meter Hobby-Eberly Telescope (hereafter, HET; [Ramsey et al. \(1998\)](#)). We used HRS with the 316g5936 cross-disperser in the 30K resolution mode with the 2 arcsecond slit and the central grating angle. This produced spectra spanning the wavelength range from 4076 – 7838 nm, although we only used the region from ~ 6600 nm redward because these M dwarf spectra suffer from low signal-to-noise at shorter wavelengths. All observations were conducted in queue mode ([Shetrone et al. 2007](#)). We exposed for 10-20 minutes per target, per epoch, based on magnitude. Wavelength calibration was obtained from ThAr frames that bracket the observation.

Spectra were extracted using a custom optimal extraction pipeline, modeled after the SpeXTool pipeline developed by [Cushing et al. \(2004\)](#) and similarly written in the Interactive Data Language (IDL). The HRS pipeline automates basic image processing procedures, such as overscan correction, bias subtraction, flat-fielding, and core spectral extraction processes such as tracing each

order, computing the optimal fiber profile, and extracting source and ThAr lamp spectra. Wavelength solutions are derived by fitting a multi-order function to the ThAr spectra using the linelist reported by ([Murphy et al. 2007](#)) and applied to the object spectra.

Extracted, wavelength calibrated spectra were then merged across areas of inter-order interlap, and trimmed to exclude regions of significant contamination by telluric absorption or OH night-sky emission lines. Regions dominated by telluric absorption were identified by inspecting the LBLRTM atmospheric model ([Clough et al. 2005](#)); sharp night-sky emission features were removed by linearly interpolating over wavelength regions known to host strong emission lines (e.g. [Abrams et al. 1994](#)).

3. BULK ANALYSIS

3.0.1. Cuts

Of the 44 sources that we identified as likely SB2s, 9 systems do not exhibit, at any epoch for which we have data, a velocity separation sufficiently large to reliably measure the RVs of both components with our initial RV extraction method. Analysis with TODCOR allowed us to recover RVs for 1 of these 9 systems, providing a sample of 36 multiples with RVs for further analysis. Seven of these 36 systems are higher order systems (6 triples and 1 quadruple) with moderate velocity separations but poorly determined RVs due to significant blending in one or more of the APOGEE observations. TODCOR analysis allowed us to recover RVs for 5 of the 6 triples; the quadruple system remains unsolved. Exclusion of the 8 poorly separated systems (see Table 2), and the two unsolved higher order multiples² leave 34 targets for which we are able to measure mass ratios.

3.1. RV extraction from APOGEE visits

Radial velocities were extracted from APOGEE CCFs for all components of each system using the procedures developed by [Fernandez et al. \(2017\)](#). We describe the process briefly here, but refer the reader to the earlier work for a detailed description. Radial velocities were extracted from each APOGEE visit CCF using a multi-step fitting process, after converting the CCF’s abscissa from lag space to velocity space.

In the first step, a Lorentzian was fit to the maximum peak of the CCF. This Lorentzian was then subtracted from the CCF, removing the primary peak. With the primary peak removed, a second Lorentzian was then fit to the maximum in the residual CCF, which was implicitly identified as the secondary peak. For sources with

² 2M10331367+3409120, 2M10520326+0032383

Table 1. Selected Binaries

2MASS ID	Phot.			CCF					Well
	Mass	Visits	R_{151}	R_{101}	R_{51}	maximum	x_{range}	Separated	
	(M_{\odot})							Epochs	
2M00372323+4950469	0.207	3	6.09	7.84	5.88	0.32	78.60	0	
2M03122509+0021585	0.109	4	6.69	7.07	6.25	0.35	52.55	0	
2M03330508+5101297 ³	0.526	3	6.52	5.75	5.04	0.54	157.74	2	
2M03393700+4531160	0.268*	6	3.75	3.28	2.88	0.59	31.36	4	
2M04281703+5521194 ¹	0.168*	13	7.60	6.75	4.96	0.42	186.37	0	
2M04373881+4650216	0.438*	4	8.60	7.20	5.19	0.66	14.90	2	
2M04595013+3638144	0.203	3	5.78	5.40	3.96	0.39	15.48	3	
2M05421216+2224407	0.178	4	5.18	4.67	3.29	0.44	14.10	1	
2M05504191+3525569	0.153*	3	6.74	5.85	4.42	0.52	48.04	1	
2M06115599+3325505 ¹	0.152	13	4.29	3.47	3.08	0.69	27.22	11	
2M06125378+2343533	0.562*	3	9.38	8.01	5.80	0.77	32.13	3	
2M06213904+3231006	0.430	6	4.19	3.54	2.67	0.68	26.13	5	
2M06561894-0835461	0.193	4	6.75	6.22	4.90	0.61	31.88	3	
2M07063543+0219287 ²	0.653*	3	5.48	4.46	3.18	0.83	7.38	1	
2M07444028+7946423	0.601*	3	3.17	2.58	3.22	0.76	13.50	2	
2M08100405+3220142	0.376	6	5.90	4.91	3.42	0.79	19.03	3	
2M08351992+1408333 ³	0.149	3	8.25	7.01	5.13	0.47	12.03	1	
2M10331367+3409120 ³	0.515	3	4.25	3.66	2.93	0.77	14.51	2	
2M10423925+1944404	0.403	4	6.76	5.70	4.10	0.50	12.47	3	
2M10464238+1626144 ¹	0.181	3	5.00	4.83	3.68	0.46	14.51	3	
2M10520326+0032383 ⁴	0.175	3	2.46	2.06	3.16	0.43	8.73	3	
2M11081979+4751217	0.191	5	4.66	4.14	2.99	0.47	107.92	5	
2M12045611+1728119 ¹	0.386	3	6.40	5.70	4.43	0.61	25.47	3	
2M12193796+2634445	0.266	8	8.76	7.97	5.98	0.38	72.52	0	
2M12214070+2707510	0.465	11	5.93	4.86	3.38	0.78	32.00	6	
2M12260547+2644385	0.926*	11	8.82	7.24	5.19	0.89	5.27	0	
2M12260848+2439315	0.348	8	4.33	3.76	2.72	0.60	53.74	7	
2M14545496+4108480	0.202	4	5.05	4.39	3.03	0.48	36.58	4	
2M14551346+4128494	0.340	4	7.45	6.28	5.30	0.70	13.67	4	
2M14562809+1648342	0.542	3	9.85	8.49	6.22	0.79	11.20	1	
2M15183842-0008235 ³	0.528*	3	5.49	4.44	3.20	0.83	10.74	1	
2M15192613+0153284 ¹	0.221	14	9.48	8.54	6.37	0.52	22.29	0	
2M15225888+3644292 ³⁵	0.644*	3	6.73	5.54	3.90	0.86	5.69	1	
2M17204248+4205070 ¹	0.158	15	7.02	6.73	5.21	0.56	24.15	12	
2M18514864+1415069	0.479*	3	10.64	8.95	6.70	0.76	30.77	0	
2M19081153+2839105	0.184	13	5.55	4.79	3.41	0.60	49.25	1	
2M19235494+3834587 ¹²	0.822*	3	3.19	2.56	2.12	0.71	34.93	1	
2M19433790+3225124	0.630*	3	8.10	6.93	5.21	0.86	28.96	1	
2M19560585+2205242	0.168	14	9.98	9.14	6.70	0.60	14.57	0	
2M20474087+3343054 ²	0.631*	3	4.87	4.11	3.16	0.83	17.71	2	
2M21005978+5103147	0.380	5	5.35	4.44	3.03	0.69	8.47	4	
2M21234344+4419277	0.494	8	4.56	3.62	4.03	0.59	21.84	7	
2M21442066+4211363 ¹	0.149*	12	2.62	4.36	3.21	0.47	62.68	12	
2M21451241+4225454	0.212	12	8.05	7.38	5.27	0.64	11.33	0	

NOTE—Stellar masses are estimated from the (V-K) vs. Mass relation derived by Delfosse et al. (2000); values tagged with a * are determined from the M_K vs. Mass relation derived by Mann et al. (2015), after adopting a distance based on a measured trigonometric parallax or a fiducial solar neighborhood distance of 20 pc.

¹ Identified by Deshpande et al. (2013) as an SB2.

² Identified by El-Badry et al. (2018a) as an SB2.

³ Found here to be an SB3.

⁴ Found here to be an SB4.

⁵ Identified by El-Badry et al. (2018a) as an SB3.

Table 2. Excluded Targets

2MASS ID	Max ΔRV ($\frac{km}{s}$)
2M00372323+4950469	22.58
2M03122509+0021585	15.13
2M04281703+5521194	30.77
2M12193796+2634445	30.05
2M15192613+0153284	28.48
2M18514864+1415069	24.97
2M19560585+2205242	40.27
2M21451241+4225454	15.04

multiple APOGEE visit spectra, the epoch containing the greatest separation between the primary and secondary peaks was identified as the “widest separated CCF”. A dual-Lorentzian model was then fit to the widest separated CCF using the peak centers identified earlier for the primary and secondary components to initialize the fit. Finally the dual-Lorentzian fit was performed on the remaining epochs using the peak heights and widths measured from the “widest separated epoch” to initialize the fit, along with the previously identified peak velocities.

A notable deficiency of this extraction method is that the resultant RVs lack an individually defined uncertainty value. Section 3.3 of F17 details their calculation of a pseudo-normal 1σ error of $\sim 1.8 \frac{km}{s}$. We adopt this ensemble uncertainty value for all RVs extracted by CCF-fitting. Another difficulty the CCF fitting method faces is consistent assignment of velocities to the primary and secondary components for SB2s with flux ratios close to unity. The accuracy of the RV values measured via this extraction technique suffered for epochs with small velocity separations, so we flagged these systems for follow up analysis with the TODCOR algorithm (Zucker & Mazeh 1994), which is more adept at extracting velocities from epochs with small velocity separations. The CCF-fit derived RVs are replaced at any epochs for which TODCOR RVs were extracted.

Figure 3 shows the Lorentzian fits to the primary and secondary peaks in all CCFs computed from APOGEE spectra of 2M17204248+4205070. Figures such as this were visually inspected to identify cases where the fits to the CCF peaks were obviously incorrect (i.e., a fit to a spurious structure in the CCF, most often occurring at epochs without well separated CCF peaks). In such cases, spurious RV measures were removed from the sample. SB2 radial velocities are listed in Table 3, which is presented here as a stub. The full version can be found in Appendix B.

Table 3. Radial Velocity Measurements of SB2s

2MASS ID	Visit	Epoch (MJD)	SDSS plate & Fiber	SNR	v_{prim} ($\frac{km}{s}$)	v_{sec} ($\frac{km}{s}$)
2M03393700+4531160	1	56195.3409	6244-56195-086	117	-16.2	33.8
	2	56200.2983	6244-56200-131	210	-20.4	38.9
	3	56223.2868	6244-56223-131	215	-37.3	53.8
	4	56196.3190	6245-56196-077	168	52.0	-36.3
	5	56202.2755	6245-56202-074	137	7.5	-
	6	56224.3188	6245-56224-077	186	11.1	3.9
2M04373881+4650216	1	56176.4835	6212-56176-050	49	-40.8	-44.4
	2	56234.3042	6212-56234-050	32	-31.5	-56.4
	3	56254.2442	6212-56254-050	62	-26.1	-63.8
	4	56260.2176	6212-56260-050	44	-26.6	-61.6
:	:	:	:	:	:	:

NOTE—Dashed out velocities indicate spurious RVs omitted from analysis. RVs not extracted via TODCOR are assigned the ensemble uncertainty of $\sim 1.8 \frac{km}{s}$.

3.2. RV extraction via TODCOR

We used the TODCOR algorithm (Zucker & Mazeh 1994) to measure RVs from all HET/HRS spectra and any APOGEE spectra flagged with low RV separations. This TODCOR analysis followed the procedures previously discussed by Bender et al. (2005) and used the algorithm implementation of Bender et al. (2012); we briefly summarize here the key parts of this implementation and its modification for use with APOGEE spec-

tra, but refer the reader to the previous presentations for more details. TODCOR simultaneously cross-correlates each target spectrum against the spectra of two template stars. For both the HRS and APOGEE observations we generated template spectra from the BT-Settl library (Allard et al. 2012), convolved to each spectrograph’s resolution and rotationally broadened using the Claret (2000) non-linear limb darkening models. Templates were optimized for each binary by maximizing the peak

correlation, using a template grid with $\Delta T_{eff} = 100K$, $\Delta \log(g) = 0.5$, and $\Delta[M/H] = 0.5$. This optimization happens independently for the HRS and APOGEE spectra. Due to variations in the quality of the linelists that underlie the BT-Settl models, we frequently derive slightly different optimal template sets for visible and near-infrared spectra. These differences are typically within one or two gridpoints (i.e., 100-200 K in temperature, and <0.5 dex in $\log(g)$ and $[M/H]$), and RVs are not sensitive to template choice at this resolution. An initial set of RVs was derived for all epochs of a given system by using the secondary-to-primary flux ratio (α) optimization of TODCOR. These RVs were then iterated with a fixed α corresponding to the average α derived for all epochs. We extract component RVs from a quadratic fit to the top six-to-eight points of the 2D cross-correlation peak, and derive uncertainties using the maximum likelihood formalism of Zucker & Mazeh (1994). We flag the epochs for which velocities were extracted from HET/HRS or APOGEE spectra using this technique.

Our analysis also revealed several triple systems composed of a short period binary along with a wider companion. We analyzed these systems with the TRICOR extension of TODCOR (Zucker et al. 1995), using three templates and solving for two independent flux ratios. The small number of epochs and relatively small temporal baselines limit what we can conclude about the stability of these systems or the orbital period of the wide component. We present the RVs derived for these candidate SB3 systems in Table 4; in all cases, the RVs derived for the wide companion are consistent within the uncertainties with the systemic RV of the inner pair, as would be expected for bound systems. Additionally, we did not detect any significant RV motion from any of the apparent wide companions. Consequently, we conclude that these are likely to be bound, hierarchical triple systems.

3.3. Mass Ratio Measurements

3.3.1. Measurement Technique

We used the method presented in Wilson (1941) to measure the mass ratios ($q \equiv \frac{M_{sec}}{M_{prim}}$) of our targets via a linear regression of primary velocity as a function of secondary velocity. Mass ratios greater than 1 were measured for 4 targets in the sample of 34 with reliably extracted RVs; we interpret these high q values as a sign of a primary/secondary assignment mismatch, and have therefore swapped the assignment for these targets, and included the resulting lower q values in the remainder of our analysis. The mass ratios measured for the 34 member sample are listed in Table 5, with Wilson plots for

each system presented in Figure 4, and the mass ratio distribution of the entire sample shown in Figure 5.

3.4. Detection limits

A detailed analysis of the selection effects introduced by the cadence of APOGEE observations and the sensitivity of our binary detection method to systems with varying mass ratios, inclinations, and separations is beyond the scope of this paper. To provide first order indicators of the biases and limits that affect the make-up of our sample, however, we calculate fiducial detection limits imposed by the requirement that we detect multiple components, well-separated in velocity space, in at least one APOGEE spectrum. It is worth noting that the ancillary science program is composed of targets of opportunity, and was not designed to be complete in distance or magnitude.

We first consider the H-band flux ratio that a system must satisfy to be detectable as a double-lined spectroscopic binary. Given the characteristic scale of the substructure in a typical APOGEE CCF, and the typical ratios of the integrated areas of the primary & secondary CCF peaks for systems identified by our detection routine, we estimate that our detection method will begin to become significantly incomplete for systems with a secondary-to-primary H-band flux ratio ≤ 0.2 , or a magnitude difference of $\Delta H \leq 1.2$. Consulting the H-band magnitudes and fluxes tabulated by Kraus & Hillenbrand (2007), we find that binaries with M dwarf primaries typically satisfy this H-band flux ratio limit if they possess a mass ratio ≥ 0.5 . To illustrate the nature of this detection limit, we show in Figure 6 the CCF of a system with a mass ratio near, but just above, this fiducial $q = 0.5$ limit.

We next consider the limits on system separation and orbital period imposed by the requirement that we detect two clearly separated CCF peaks. Given the resolution of the APOGEE spectrograph, a system's CCF peaks are clearly separated for primary-secondary velocity separations of $\Delta RV_{lim} \sim 30 \text{ km s}^{-1}$ or more (Fernandez et al. 2017). This velocity separation threshold imposes a joint constraint on the inclination (i), total mass ($M_1 + M_2$) and orbital period (P) of systems in our sample:

$$P \leq \frac{2 \pi G (M_1 + M_2) \sin^3 i}{\Delta RV_{lim}^3}$$

Expressing this constraint in terms of the system's semi-major axis (a), rather than its orbital period, makes this limit:

$$a \leq \frac{G (M_1 + M_2) \sin^3 i}{\Delta RV_{lim}^2}$$

Table 4. Radial Velocity Measurements of SB3s

2MASS ID	Visit	Epoch (MJD)	SDSS plate & Fiber	SNR	$v_{prim}(\frac{km}{s})$	σ_{prim}	$v_{sec}(\frac{km}{s})$	σ_{sec}	$v_{ter}(\frac{km}{s})$	σ_{ter}
2M03330508+5101297	1	56257.1757	6538-56257-087	42	30.86	0.53	-84.72	1.57	-11.49	1.02
	2	56261.1912	6538-56261-088	73	-65.39	0.30	78.53	0.99	-10.98	0.73
	3	56288.1033	6538-56288-069	39	-14.83	0.47	-4.44	1.10	-10.48	0.93
2M04595013+3638144	1	56256.2342	6542-56256-294	43	-29.49	0.39	33.45	1.52	-10.06	0.53
	2	56262.2454	6542-56262-187	44	-33.77	0.46	39.26	1.43	-10.74	0.59
	3	56288.1841	6542-56288-192	52	-33.04	0.44	38.62	1.47	-8.80	0.71
2M08351992+1408333	1	56284.3821	6612-56284-106	248	37.04	0.36	-17.11	0.84	17.30	0.48
	2	56290.5157	6612-56290-105	246	5.62	0.42	27.05	1.19	18.66	0.53
	3	56315.3140	6612-56315-105	234	-0.02	0.39	33.29	0.79	20.10	0.42
2M15183842-0008235	1	56080.2737	5906-56080-244	235	6.30	0.27	-86.25	0.63	-36.58	0.30
	2	56435.2488	5906-56435-244	241	-46.42	0.19	-18.39	0.42	-37.26	0.24
	3	56467.1400	5906-56467-256	248	-41.37	0.28	-23.34	0.50	-35.66	0.26
2M15225888+3644292	1	56735.3805	5756-56735-106	152	-68.10	0.43	-19.08	2.10	-56.64	0.74
	2	56740.4314	5756-56740-009	185	-82.70	0.24	8.13	2.50	-57.52	0.50
	3	56762.3135	5756-56762-010	157	-15.30	0.30	-136.30	1.70	-55.46	0.60

NOTE—All velocities in this table were extracted via TODCOR.

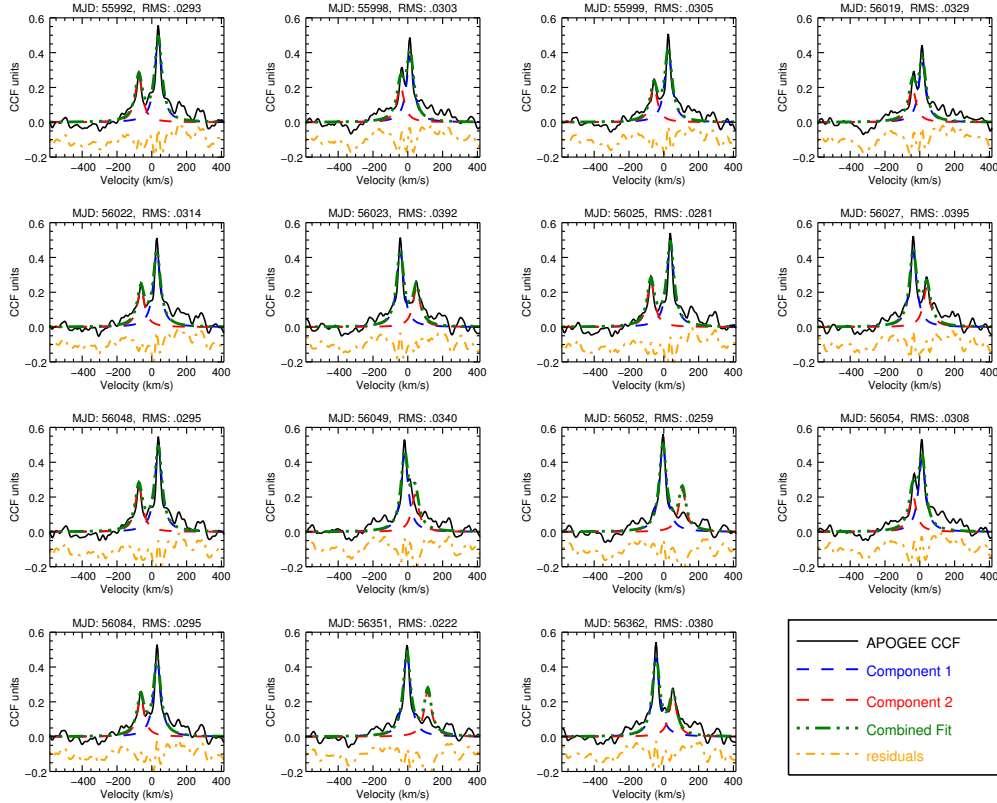


Figure 3. APOGEE CCFs for 2M17204248+4205070, transformed from lag units into velocity space. The blue and red dashed lines represent the Lorentzian fits to the primary and secondary velocity peaks, respectively; the sum of the two fits is shown as a green dashed-dotted line, and the residuals of the fit are shown as an orange dashed line, offset by 0.1 for clarity. Note the spurious secondary fits in the third and fourth rows, at epochs with MJDs of 56049, 56052 and 56351. Erroneous velocity values associated with spurious fits such as these have been removed from our dataset by visual inspection.

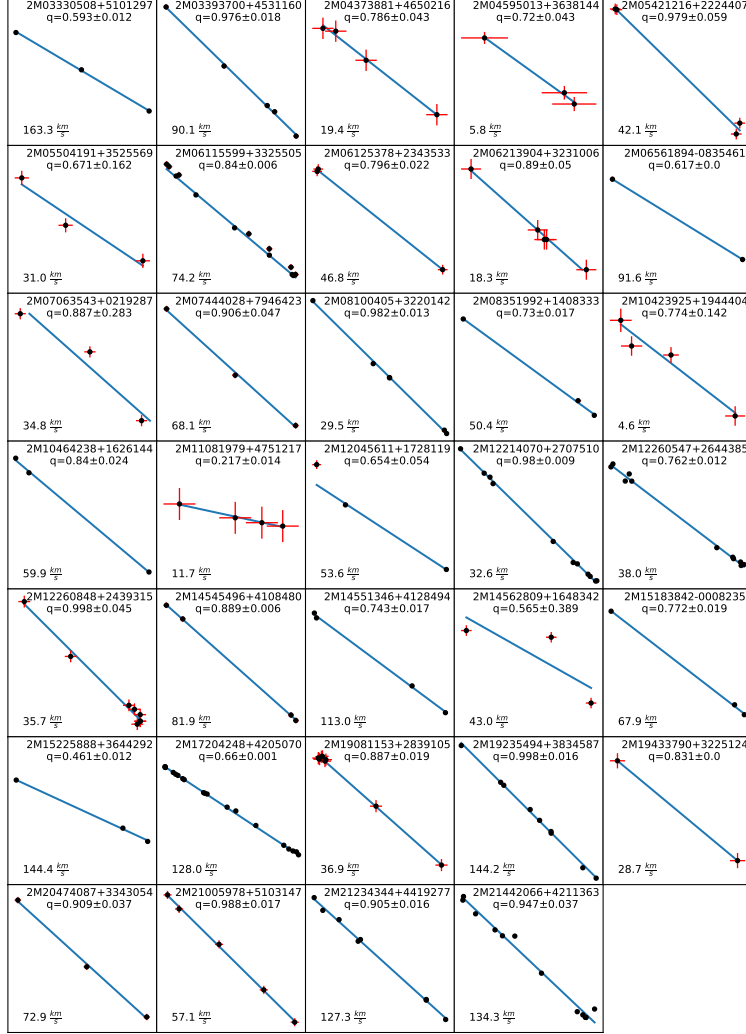


Figure 4. Wilson plots of each mass ratio measurement in our sample. The black circles are radial velocity observations. Uncertainties are shown as red bars. The blue line of each plot is best fit line to the data, from which the mass ratio is calculated. The horizontal axis is v_{sec} , the vertical axis is v_{prim} . The aspect ratio between the vertical and horizontal axes of each subplot is 1. In the lower left corner of each subplot the v_{sec} range is given.

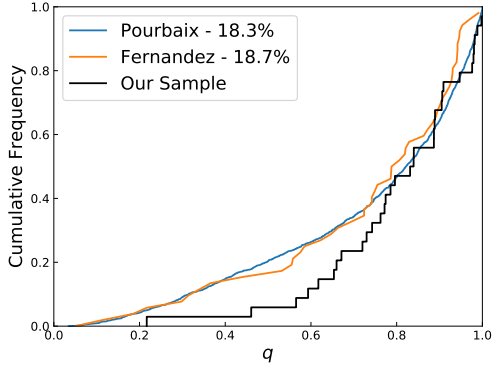


Figure 5. Mass ratio distribution of our sample, and the Kolmogorov-Smirnov statistics comparing our distribution and those of Pourbaix et al. (2004) and Fernandez et al. (2017)

Table 5. Mass ratio and ΔRV of analyzed stars

2MASS ID	$q \pm \delta q$	$\frac{\delta q}{q}$	Max ΔRV
2M03330508+5101297	0.593 ± 0.012	0.020	143.92
2M03393700+4531160	0.976 ± 0.018	0.018	91.13
2M04373881+4650216	0.786 ± 0.043	0.054	37.69
2M04595013+3638144	0.720 ± 0.043	0.060	73.03
2M05421216+2224407	0.979 ± 0.059	0.060	41.65
2M05504191+3525569	0.671 ± 0.162	0.241	37.27
2M06115599+3325505	0.840 ± 0.006	0.008	70.40
2M06125378+2343533	0.796 ± 0.022	0.028	42.88
2M06213904+3231006 ¹	0.890 ± 0.050	0.044	86.97
2M06561894-0835461 ²	$0.617 \pm -$	-	82.85
2M07063543+0219287 ¹	0.887 ± 0.283	0.251	57.98
2M07444028+7946423 ¹	0.906 ± 0.047	0.042	91.12
2M08100405+3220142	0.982 ± 0.013	0.013	34.01
2M08351992+1408333	0.730 ± 0.017	0.024	54.15
2M10423925+1944404	0.774 ± 0.142	0.184	29.56
2M10464238+1626144	0.840 ± 0.024	0.028	68.10
2M11081979+4751217	0.217 ± 0.014	0.066	64.32
2M12045611+1728119	0.654 ± 0.054	0.082	141.45
2M12214070+2707510 ¹	0.980 ± 0.009	0.009	42.65
2M12260547+2644385	0.762 ± 0.012	0.016	40.54
2M12260848+2439315	0.998 ± 0.045	0.045	41.42
2M14545496+4108480	0.889 ± 0.006	0.007	99.39
2M14551346+4128494	0.743 ± 0.017	0.023	99.42
2M14562809+1648342	0.565 ± 0.389	0.688	53.92
2M15183842-0008235	0.772 ± 0.019	0.025	92.55
2M15225888+3644292	0.461 ± 0.012	0.025	121.00
2M17204248+4205070	0.660 ± 0.001	0.002	110.28
2M19081153+2839105	0.887 ± 0.019	0.022	47.71
2M19235494+3834587	0.998 ± 0.016	0.016	161.26
2M19433790+3225124 ²	$0.831 \pm -$	-	58.67
2M20474087+3343054	0.909 ± 0.037	0.041	76.92
2M21005978+5103147	0.988 ± 0.017	0.017	57.22
2M21234344+4419277	0.905 ± 0.016	0.018	124.27
2M21442066+4211363	0.947 ± 0.037	0.039	124.23

¹ For these targets $q > 1$. We assume this is due to a primary/secondary mismatch, and report q^{-1} as q

² Only two epochs were usable for these targets, therefore δq is not well defined.

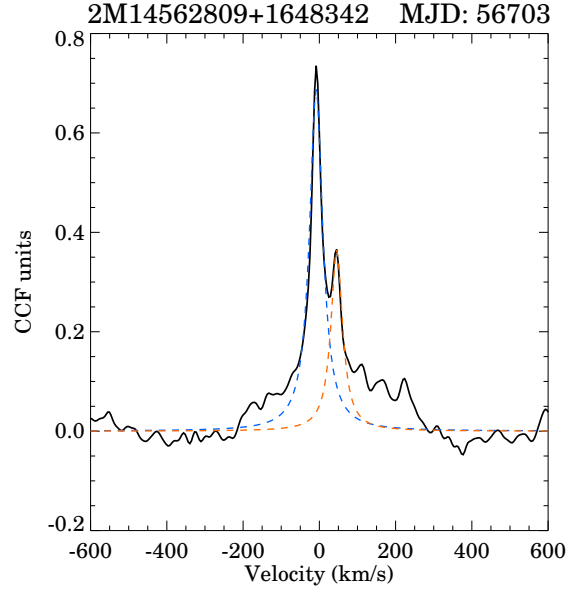


Figure 6. An APOGEE CCF for 2M14562809+1648342, a binary whose mass ratio ($q = 0.565$) places it near the fiducial $q = 0.5 / \Delta H = 1.2$ limit that we estimate for where our search method will become substantially incomplete due solely to the inability to confidently detect the secondary companion, even at high velocity separations.

Edge-on ($i \sim 90^\circ$), equal-mass systems are the most favorable configuration for detection: for a fiducial pair of $0.5 M_\odot$ stars, we find a limiting period of ~ 1 year and a limiting separation of 1 AU; for a lower mass pair of $0.25 M_\odot$ stars, we find a limiting period and separation of ~ 0.5 years & AU, respectively³. Due to the $\sin^3 i$ term in these limits, however, these limits decrease quickly with inclination: a modest inclination of 30° reduces the detection limits for the $0.5 M_\odot$ binary to ~ 0.12 years and AU, and to 0.06 years and AU for the $0.25 M_\odot$ system.

The considerations above demonstrate that our sample is biased towards edge-on systems with mass ratios ≥ 0.5 , and will be most complete for systems with characteristic periods and separations of ≤ 0.1 years and ≤ 0.1 AUs. We therefore adopt 0.1 years and 0.1 AUs as useful benchmarks for the completeness limits of our observed sample, and for comparing the properties of this sample to those measured from other samples of binary stars reported in the literature.

³ As years and AUs are defined based on the properties of our own solar system, and scale identically with system mass and inclination, the limiting period and separation for a fiducial system will be numerically identical when expressed in units of years and AUs

4. FULL ORBIT FITS FOR HIGH VISIT, HIGH ΔRV SYSTEMS

4.1. Criteria for full orbital fits

The choice of targets chosen for orbital fits was made using the 3 following criteria, met by 4 systems:

- Primary and secondary RVs for at least 8 visits.
- Fractional mass ratio uncertainty less than 10%.
- V_{cov} value of at least 0.7, where V_{cov} is the velocity coverage statistic presented in equation 5 of Fernandez et al. (2017).

$$V_{cov} = \frac{N}{N-1} \left(1 - \frac{1}{RV_{span}^2} \sum_{i=1}^N (RV_{i+1} - RV_i)^2 \right)$$

With N equal to the number of visits, and $RV_{span} = RV_{max} - RV_{min}$.

4.2. Fitting procedure

Radial velocities expected for each component were calculated from a model consisting of 6 parameters: velocity semi-amplitude of the primary (K), eccentricity (e), longitude of periastron (ω), time of periastron (T), orbital period (P), and barycenter velocity (γ). A model radial velocity curve was computed, starting with the mean anomaly, M :

$$M = \frac{2\pi}{P} (t - T)$$

Using M , the eccentric anomaly, E is computed:

$$E = M + e \sin(M) + e^2 \frac{\sin(2M)}{2}$$

Using E , the true anomaly ν is computed:

$$\nu = 2 \arctan \left(\sqrt{\frac{1+e}{1-e}} \cdot \tan \left(\frac{E}{2} \right) \right)$$

and finally the primary and secondary radial velocities were calculated:

$$vel_{prim} = K [\cos(\nu + \omega) + e \cos(\omega)] + \gamma$$

$$vel_{sec} = -\frac{K}{q} [\cos(\nu + \omega) + e \cos(\omega)] + \gamma$$

q was treated as a constant for each system, its value inherited from the method presented in §3.2

The set of orbital parameters $\theta \equiv (K, e, \omega, T, P, \gamma)$ which accurately predicts the observed radial velocities of each component represents a possible orbital solution for the system. To find the best orbital fit we explored

this parameter space using Bayesian techniques. We sampled the parameter space using *emcee* (Foreman-Mackey et al. 2013), a Python implementation of an affine invariant ensemble sampler (Goodman 2010). We used an ensemble of 4000 walkers, distributed evenly throughout the space, for 2000 steps. We kept the final 1000 steps of each run, discarding the initial 1000 as a burn-in phase.

For the number of visits typical of our orbital solutions (on the order of 10), the posterior probability distributions of P were multimodal and highly degenerate. This made a period determination difficult. To perform the period search, we probed the parameter space using a modified likelihood function. The likelihood p of observing the dataset y given θ was defined:

$$p(y|\theta) = \exp \left[-\sqrt{\frac{1}{N} \sum_{i=1}^N \frac{(o_i - c_i)^2}{\sigma_i} prim + \frac{(o_i - c_i)^2}{\sigma_i} sec} \right]$$

where o_i is the i^{th} observation in y and c_i is the computed radial velocity based on θ at the i^{th} epoch. This definition prevents the ensemble from converging tightly on any single local maximum, allowing for multiple modes to be explored in a single walk. Figure 7 shows an example of the results of the MCMC period search using this likelihood definition, overlaid with a Lomb-Scargle periodogram. In Figure 7, the samples are densest in period space at 3.29 days, corresponding to a peak in periodogram power. We define a period confidence, \mathcal{L} , as the fraction of MCMC samples contained within the primary peak identified by the period search: in the case shown in Figure 7, $\mathcal{L} = 30\%$. The highest period confidence value we measure is 79%, for 2M21442066+4211363; for the other three systems, we measure period confidence values ranging from 16–56%, suggesting that the maximum likelihood period is probable, but not yet definitively measured. The MCMC analysis also appears to favor shorter periods for these systems, producing a potential bias for other values inferred from the period measurements.

After constraining the period, we adopt the following priors for the other 5 parameters:

- $0 < K < 100 \frac{km}{s}$
- $0 < e < 0.8$
- $0 < \omega < 2\pi$
- $(\text{median JD} - \frac{P}{2}) < T < (\text{median JD} + \frac{P}{2})$
- $\text{min. observed RV} < \gamma < \text{max. observed RV}$

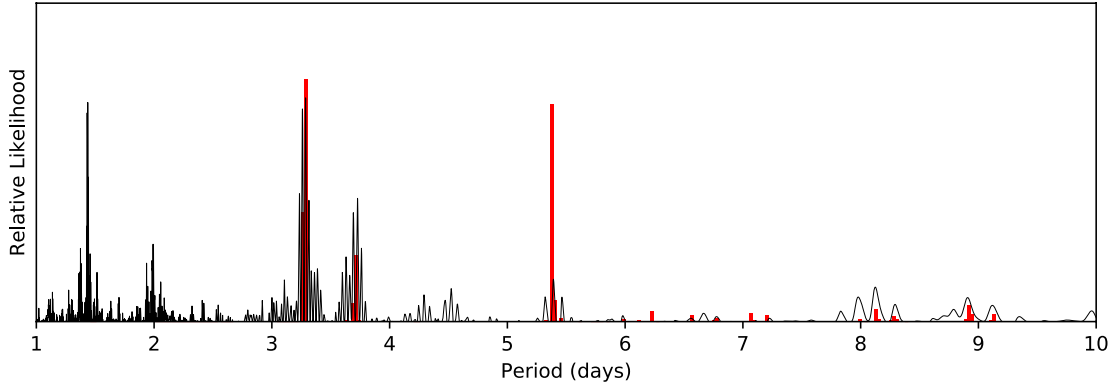


Figure 7. Periodogram power as a function of period (black), and a histogram of period samples drawn from the MCMC process (red) for 2M17204248+4205070.

In the random walk for the full orbital solution, we use the likelihood function:

$$p(y|\theta) = \exp \left[- \sum_{i=1}^N \frac{(o_i - c_i)^2}{2\sigma_i} \text{prim} + \frac{(o_i - c_i)^2}{2\sigma_i} \text{sec} \right]$$

This likelihood function reflects our assumption of independent, Gaussian probabilities. For cases when the ensemble converged toward $e = 0$, we performed a second run with a slightly modified circular orbit model, in which both e and ω were constrained to 0. For each orbit fit, our choice of model was consistent with the Bayesian Information Criterion.

We report the 50th quantile of the post burn-in distribution of the converged walkers as the value of each parameter. As uncertainties, we report the 16th and 84th quantiles as quasi 1σ values.

As a check against our orbital solutions, we estimate a lower bound on primary mass in Table 6 (See Appendix A for the derivation). All dynamical lower mass limits are significantly lower (by a factor of 5-10) than the photometric mass estimate of the primary listed in Table 1. This indicates that either the sample includes an anomalously large number of high inclination systems, such that their dynamical mass is a significant underestimate of their true mass, or that the orbital period we have inferred is underestimated, as the dynamical mass estimate scales linearly with the system’s assumed orbital period. We suspect the latter explanation is more likely, and suggest that additional monitoring of these systems to remove the uncertainty that remains in the systems’ periods is necessary.

5. RESULTS

Frequency: As noted earlier, the systems which we detect as close multiples are a biased and incomplete subset of the larger, true population of close multiples within the parent sample of the SDSS-III/APOGEE M

dwarf ancillary sample. Nonetheless, it is instructive to compare the raw multiplicity fraction that we infer from this sample to prior measurements of the frequency of close companions to M-type primaries. Fischer & Marcy (1992) (FM1992) and Clark et al. (2012) (CBK2012) analyzed RV variability in multi-epoch optical spectra to infer a close ($a < 0.4$ AU) binary fraction of $1.8 \pm 1.8\%$ and 3-4%, respectively. More recently, Shan et al. (2015) analyzed the population of M+M eclipsing binaries in the Kepler field to infer a frequency of $11 \pm 2\%$ for close ($P < 90$ days, or $a \leq 0.25$ AU for a fiducial $0.5 + 0.5 M_{\odot}$ system) companions to M dwarf primaries.

The raw (i.e., without corrections for incompleteness, inclination bias, etc.) binary fraction that we measure in our APOGEE sample ($\sim 3\%$; $37/1350 = 2.74\%$) seems to match the frequencies inferred by FM1992 and CBK2012. Those prior measurements have been corrected for incompleteness and selection effects, however, while our raw multiplicity fraction has not. The only selection effect that would drive our raw multiplicity fraction to overestimate the true value is the magnitude limited nature of the APOGEE M dwarf ancillary targets; biases due to inclination, flux ratios, and temporal sampling will all conspire to make our empirically measured rate underestimate the true multiplicity fraction. Thus, our measurement should be an underestimate of the true intrinsic multiplicity fraction. If completeness correction shows that our current binary detection rate is above 50%, then our result would support that of FM1992 and CBK2012. If our current binary detection rate is below 50%, then our result would more strongly favor Shan et al. (2015). Detailed modeling will be necessary to draw strong conclusions, and should be the subject of future work.

Mass Ratio Distribution: Measuring the mass ratios of 29 M Dwarf SB2s and 5 SB3s, we find a mass ratio distribution that reaches as low as 0.217, but with

Table 6. Orbital fits

	2M06115599+3325505	2M17204248+4205070	2M21234344+4419277	2M21442066+4211363
K	32.29 ± 0.14	43.87 ± 0.08	58.51 ± 0.59	61.16 ± 0.46
e	0.01 ± 0.003	0.002 ± 0.002	0.062 ± 0.0012	0
ω	$128.94^{+30.75}_{-39.84}$	$54.47^{+39.25}_{-25.77}$	$127.78^{+8.69}_{-9.00}$	0
T	261.7467 ± 0.006	$49.3840^{+0.3583}_{-0.2350}$	$488.0751^{+0.1982}_{-0.2036}$	205.3381 ± 0.0057
$P(\mathcal{L})$	2.63(56%)	3.29(30%)	8.17(16%)	3.30(79%)
γ	76.98 ± 0.06	-6.77 ± 0.05	-123.59 ± 0.45	-17.22 ± 0.37
$\frac{M_{prim}^a}{M_{\odot}}$	0.005	0.017	0.089	0.04

NOTE—Units are $K(\frac{km}{s})$, $\omega(\text{degrees})$, $T(\text{JD}-2456000)$, $P(\text{days})$, $\gamma(\frac{km}{s})$.

^a dynamical minimum mass estimates for the system’s primary component, derived as explained in Appendix A. The minimum mass of an M dwarf primary is $M \geq 0.075M_{\odot}$; individual photometric mass estimates for each primary are listed in Table 1, with a range of 0.15-0.49 M_{\odot} .

most systems having mass ratios between 0.8 and 1. As noted in section 3.4, requiring the detection of spectral counterparts for both components of the system will bias our sample towards equal mass ratios. Nonetheless, it is again instructive to compare our mass ratio distribution to those measured in existing samples of SB2s, particularly as those catalogs will suffer from similar selection biases. Our cumulative mass ratio distribution shows fair agreement to those found by Pourbaix et al. (2004) and Fernandez et al. (2017): while our mass ratio distribution appears somewhat more strongly skewed towards equal mass systems, a Kolmogorov-Smirnov test finds a $\sim 18\%$ chance that the mass ratio distribution that we measure for the APOGEE M dwarf SB2s is consistent with those measured Pourbaix et al. (2004) and Fernandez et al. (2017) for similarly biased catalogs of (higher mass) SB2s.

Orbits: Orbital fit results are tabulated in Table 6. All 4 orbital solutions exhibit small eccentricities ($e < 0.1$). We find periods of 2.6-8.2 days. In the context of a multimodal period distribution, defining uncertainty via peak width is problematic. As a result, we omit uncertainties on our measurement of orbital period in favor of the period confidence defined in §4.2. Three key figures (see Figures 8-11) are included for each orbital solution, following §6.

6. CONCLUSIONS

1. We have identified 44 candidate close multiple systems among the 1350 targets in the SDSS-III/APOGEE M dwarf ancillary sample. These candidates include 8 of the 9 SB2s previously identified by Deshpande et al. (2013) in their analysis of a subset of the APOGEE M dwarf sample, as well as 3 SB2s and an SB3 identified by El-Badry et al. (2018a) in their search for binaries

within DR14, indicating that our algorithm successfully recovers close binaries whose APOGEE spectra capture an epoch where the system exhibits a large velocity separation.

2. We have extracted RVs for components in 34 of these systems, including 5 systems that appear to be higher order multiples. In most cases, these RV measurements are obtained by fitting peaks in the CCFs produced by the APOGEE reduction and analysis pipeline; in systems with more than two components, or with velocity separations too small to resolve in the APOGEE CCF, we have extracted RVs using the TODCOR algorithm on the APOGEE spectra themselves. For two stars, we have also obtained follow-up spectroscopy with the High Resolution Spectrograph on the Hobby-Eberly Telescope; we analyze these optical/far-red data using the TODCOR routine as well.
3. We fit primary and secondary RVs to measure mass ratios for the closest pair of each of the 34 systems for which we extract RVs. The mass ratio distribution of close pairs in our sample skews towards equal mass systems, and includes only one system with a mass ratio < 0.45 ; this is consistent with first order estimates of the bias towards higher mass ratios that should result from requiring a positive spectroscopic detection of both primary and secondary components. Nonetheless, the (biased and incomplete) mass ratio distribution that we measure from the M dwarf sample is consistent at the 1σ level with the mass ratio distributions reported in the literature for similarly biased samples of younger and more massive stars, suggesting that the mass ratios of close multiples are not a strong function of primary mass.

4. The low periods we measure for our targets ($P < 10$ days) are consistent with the small separations we expect for M Dwarf SB2s. The low eccentricities we measure ($e < 0.1$) reflect the tidal interactions to which close binaries are subject. Our orbit fits exhibit small residuals, excluding third bodies down to very low masses.

ACKNOWLEDGEMENTS

J.S., K.R.C., and M.K. acknowledge support provided by the NSF through grant AST-1449476, and from the Research Corporation via a Time Domain Astrophysics Scialog award. C.F.B. and N.R. acknowledge support provided by the NSF through grant AST-1517592. N.D. acknowledges support for this work from the NSF through grant AST-1616684.

Funding for SDSS-III has been provided by the Alfred P. Sloan Foundation, the Participating Institutions, the National Science Foundation, and the U.S. Department of Energy Office of Science. The SDSS-III web site is <http://www.sdss3.org/>.

SDSS-III is managed by the Astrophysical Research Consortium for the Participating Institutions of the SDSS-III Collaboration including the University of Arizona, the Brazilian Participation Group, Brookhaven National Laboratory, Carnegie Mellon University, University of Florida, the French Participation Group, the German Participation Group, Harvard University, the Instituto de Astrofísica de Canarias, the Michigan State/Notre Dame/JINA Participation Group, Johns Hopkins University, Lawrence Berkeley National Laboratory, Max Planck Institute for Astrophysics, Max Planck Institute for Extraterrestrial Physics, New Mexico State University, New York University, Ohio State University, Pennsylvania State University, University of Portsmouth, Princeton University, the Spanish Participation Group, University of Tokyo, University of Utah, Vanderbilt University, University of Virginia, University of Washington, and Yale University.

D.A.G.H. was funded by the Ramón y Cajal fellowship number RYC-2013-14182. D.A.G.H. and O.Z. acknowledge support provided by the Spanish Ministry of Economy and Competitiveness (MINECO) under grant AYA-2014-58082-P.

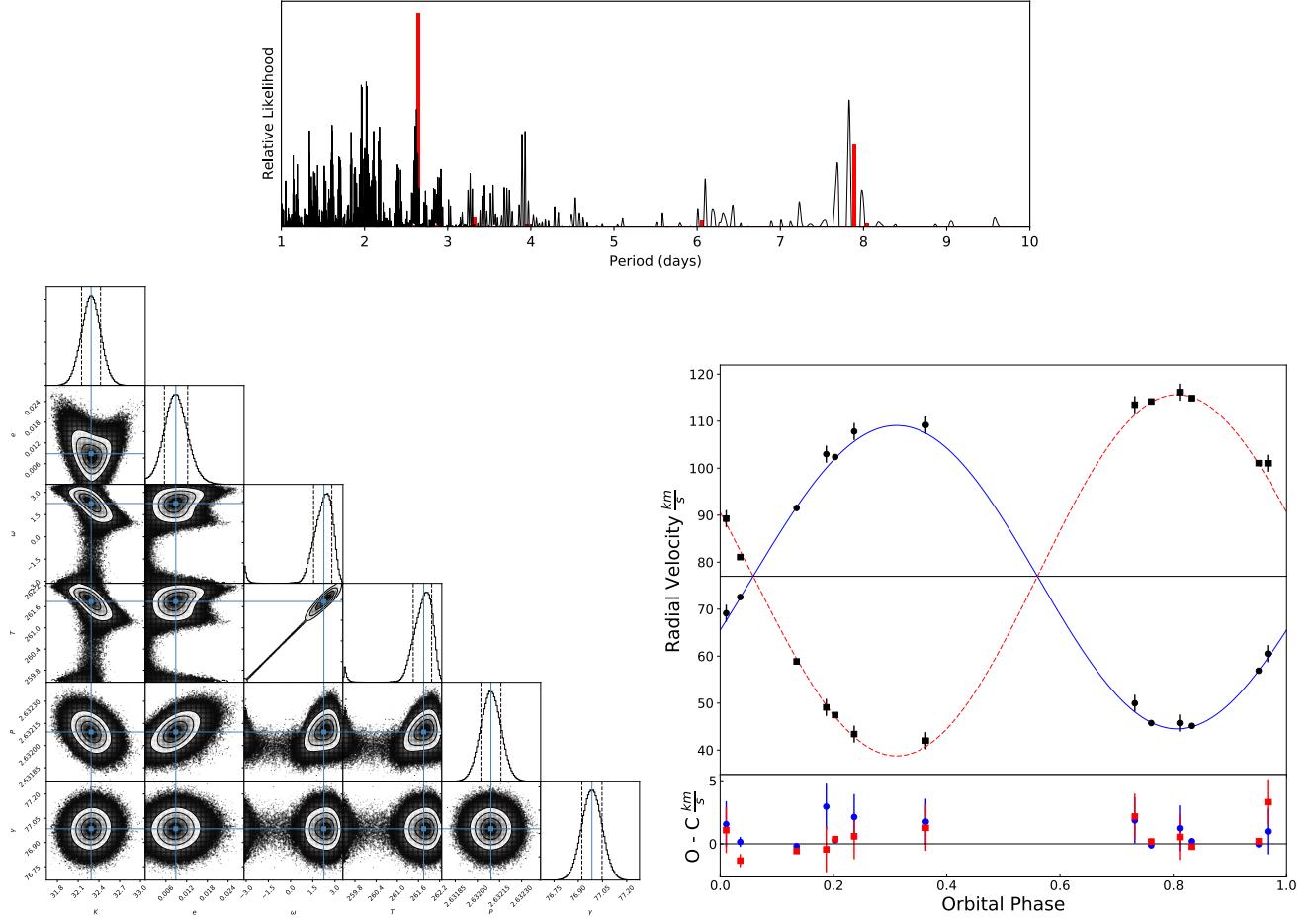


Figure 8. Figures for 2M06115599+3325505. $\mathcal{L} = 56\%$ at $P = 2.63$ days.

[Top] Lomb-Scargle Periodogram power as a function of period (black), and the histogram of MCMC samples obtained during the period search (red).

[Left] Corner plot of the posterior probability distribution given by the random walk.

[Right] Radial velocity plot of this system. The solid blue curve is the primary component velocity, and the red dashed curve is the secondary component velocity. Primary component velocities are marked as squares, secondary velocities are marked as circles.

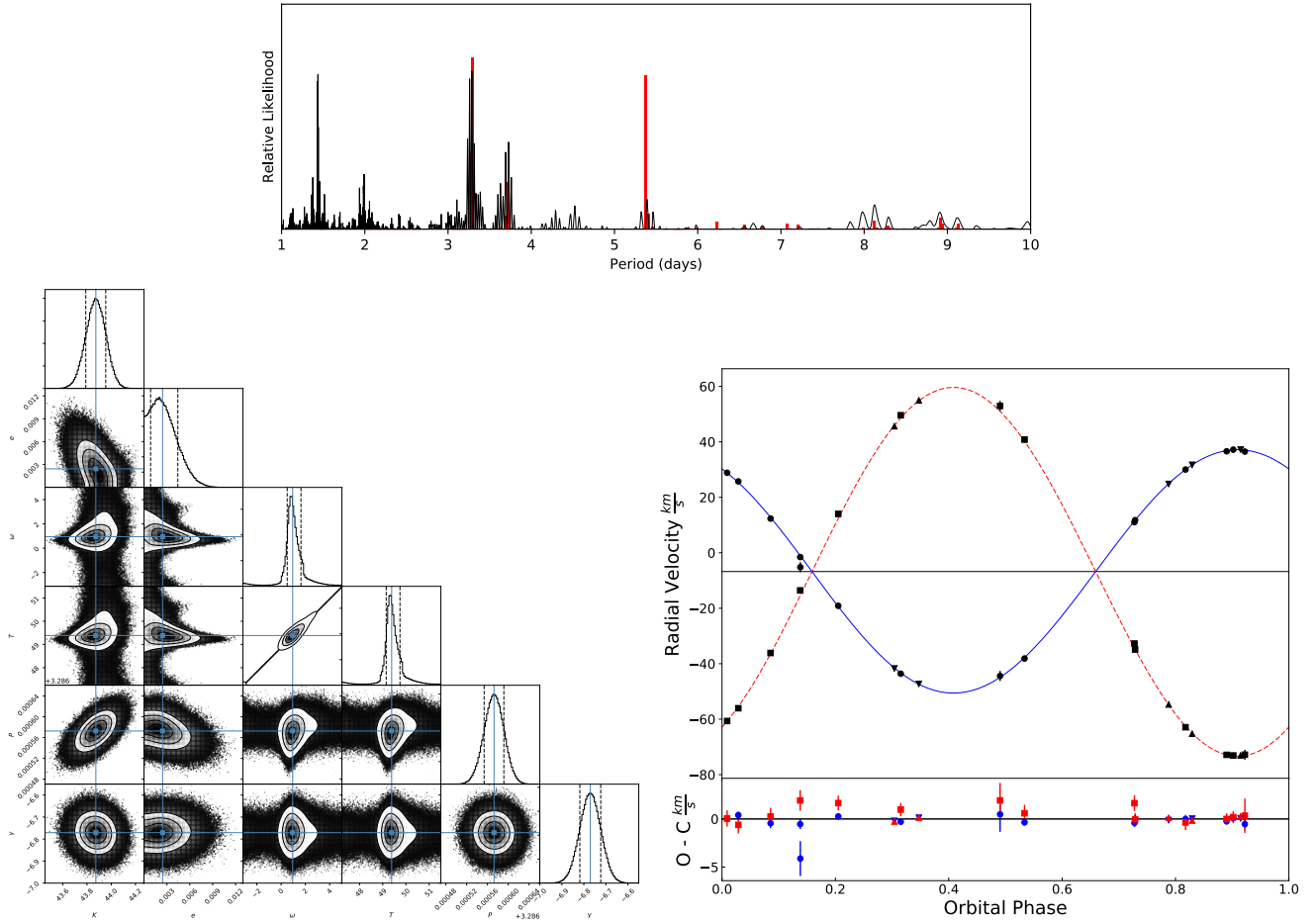


Figure 9. Figures for 2M17204248+4205070. $\mathcal{L} = 30\%$ at $P = 3.29$ days.

[Top] Lomb-Scargle Periodogram power as a function of period (black), and the histogram of MCMC samples obtained during the period search (red).

[Left] Corner plot of the posterior probability distribution given by the random walk.

[Right] Radial velocity plot of this system. The solid blue curve is the primary component velocity, and the red dashed curve is the secondary component velocity. Primary component velocities are marked as squares, secondary velocities are marked as circles.

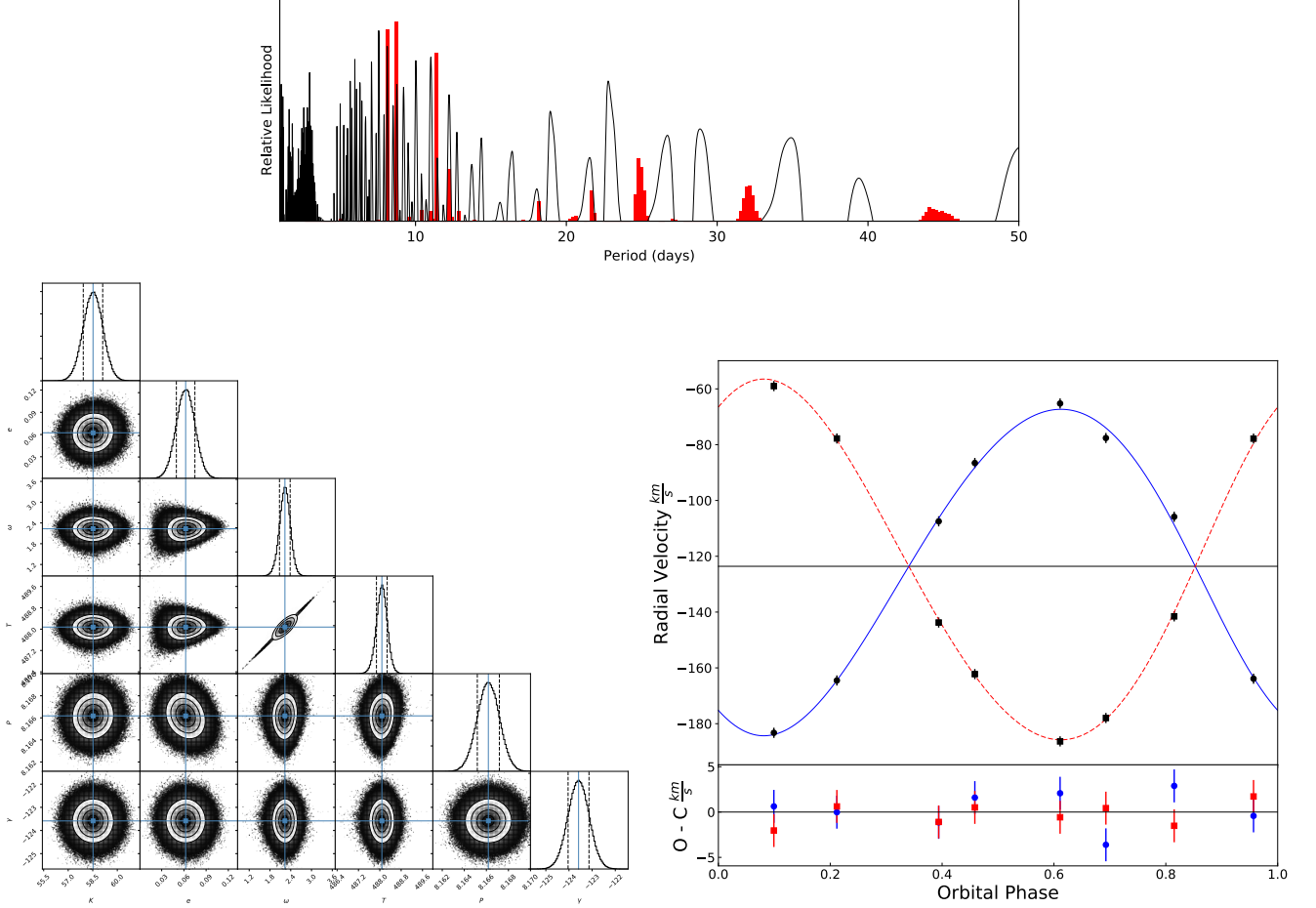


Figure 10. Figures for 2M21234344+4419277. $\mathcal{L} = 16\%$ at $P = 8.17$ days.

[Top] Lomb-Scargle Periodogram power as a function of period (black), and the histogram of MCMC samples obtained during the period search (red).

[Left] Corner plot of the posterior probability distribution given by the random walk.

[Right] Radial velocity plot of this system. The solid blue curve is the primary component velocity, and the red dashed curve is the secondary component velocity. Primary component velocities are marked as squares, secondary velocities are marked as circles.

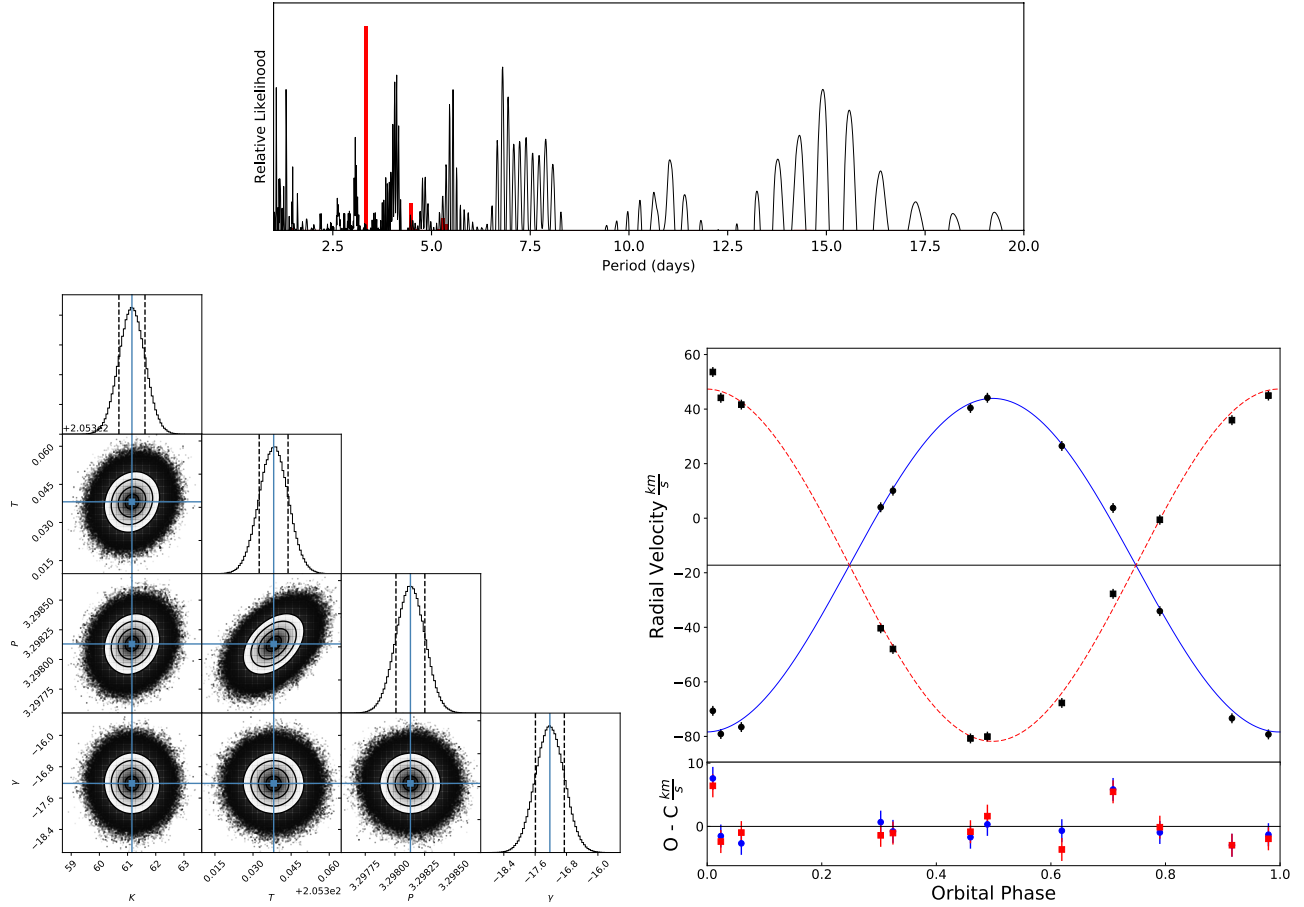


Figure 11. Figures for 2M21442066+4211363. $\mathcal{L} = 79\%$ at $P = 3.30$ days.

[Top] Lomb-Scargle Periodogram power as a function of period (black), and the histogram of MCMC samples obtained during the period search (red).

[Left] Corner plot of the posterior probability distribution given by the random walk.

[Right] Radial velocity plot of this system. The solid blue curve is the primary component velocity, and the red dashed curve is the secondary component velocity. Primary component velocities are marked as squares, secondary velocities are marked as circles.

APPENDIX

A. ESTIMATE OF PRIMARY MASS LOWER BOUND

Given that all stars in our sample are known to be M Dwarfs from their spectral information, we know that any calculated lower limit on the mass of the primary component must not fall above about $0.5M_{\odot}$. This calculation acts as an independent check on the orbital fit, which is useful given the solution degeneracy that is prevalent along the period axis.

Isolate P^2 from Newton's formulation of Kepler's 3rd law

$$P^2 = (2\pi)^2 \frac{a^3}{GM_{prim}(1+q)}$$

and an approximate expression of mean orbital speed

$$v_o \approx \frac{2\pi a}{P} \left[1 - \frac{1}{4}e^2 - \frac{3}{64}e^4 \right]$$

where $v_o \approx K$. This approximation is sufficiently accurate for low e , and pushes the estimate down for non-zero e . Edge-on orientation is assumed, firmly establishing this calculation as a lower bound on primary mass.

$$K \leq \frac{2\pi a}{P} \left[1 - \frac{1}{4}e^2 - \frac{3}{64}e^4 \right]$$

substitution and simplification ultimately gives

$$M_{prim} \geq \frac{K^3 P}{2\pi G(1+q) \left[1 - \frac{1}{4}e^2 - \frac{3}{64}e^4 \right]^3}$$

If the orbital solution places this value significantly above $0.5M_{\odot}$, then it cannot be a correct solution.

B. DATA TABLES

The list of SB2 Radial Velocity measurements is given here in its entirety.

Table 7. Radial Velocity Measurements of SB2s

2MASS ID	Visit	Epoch (MJD)	SDSS plate & Fiber	SNR	$v_{prim}(\frac{km}{s})$	$v_{sec}(\frac{km}{s})$
2M03393700+4531160	1	56195.3409	6244-56195-086	117	-16.2	33.8
	2	56200.2983	6244-56200-131	210	-20.4	38.9
	3	56223.2868	6244-56223-131	215	-37.3	53.8
	4	56196.3190	6245-56196-077	168	52.0	-36.3
	5	56202.2755	6245-56202-074	137	7.5	-
	6	56224.3188	6245-56224-077	186	11.1	3.9
2M04373881+4650216	1	56176.4835	6212-56176-050	49	-40.8	-44.4
	2	56234.3042	6212-56234-050	32	-31.5	-56.4
	3	56254.2442	6212-56254-050	62	-26.1	-63.8
	4	56260.2176	6212-56260-050	44	-26.6	-61.6
2M05421216+2224407	1	56291.1826	6761-56291-131	25	10.0	49.2
	2	56559.4916	6761-56559-134	78	6.3	48.0
	3	56582.4342	6761-56582-128	88	48.6	7.1
	4	56586.4264	6761-56586-128	69	48.4	7.6
2M05504191+3525569	1	56262.3018	6543-56262-287	95	83.0	69.1
	2	56285.1795	6543-56285-284	37	73.9	88.9
	3	56313.1350	6543-56313-296	80	95.1	57.8
2M06115599+3325505	1 ¹	55848.4441	5508-55848-274	157	45.16±0.19	114.89±0.25
	2 ¹	55849.4183	5507-55849-220	131	102.38±0.18	47.46±0.23
	3 ¹	55927.2179	5507-55927-226	110	45.76±0.19	114.19±0.25
	4 ¹	55928.2021	5508-55928-219	181	91.53±0.17	58.87±0.21
	5 ¹	55933.2042	5507-55933-219	161	72.58±0.40	81.08±0.52
	6 ¹	55967.1987	5508-55967-220	150	56.89±0.17	101.07±0.23
	7	56260.4457	6344-56260-226	202	109.2	42.0
	8	56267.4147	6344-56267-225	157	69.1	89.3
	9	56288.3556	6344-56288-225	21	60.5	101.1
	10	56314.2669	6344-56314-225	200	45.8	116.2
	11	56290.3703	6345-56290-219	153	50.0	113.5
	12	56315.2574	6345-56315-220	161	103.0	49.1
	13	56323.2832	6345-56323-220	144	107.8	43.4
2M06125378+2343533	1	56347.1522	6548-56347-027	94	1.0	-41.5
	2	56352.1825	6548-56352-021	88	1.8	-41.1
	3	56623.4989	6548-56623-015	95	-35.7	5.3
2M06213904+3231006	1	56260.4457	6344-56260-084	85	50.9	-23.4
	2	56267.4147	6344-56267-084	65	49.3	-21.6
	3	56314.2669	6344-56314-031	66	14.9	-
	4	56290.3703	6345-56290-080	56	50.5	-23.3
	5	56315.2574	6345-56315-065	62	58.1	-28.8
	6	56323.2832	6345-56323-062	49	37.2	-10.5
2M06561894-0835461	1	56587.4858	6535-56587-178	244	0.4	-
	2	56593.4881	6535-56593-171	199	-36.9	-
	3	56616.3926	6535-56616-159	68	-29.9	53.0
	4	56637.3386	6535-56637-154	217	26.7	-38.6
2M07063543+0219287	1 ²	56673.2300	6552-56673-250	229	85.72	66.91

Table 7 continued

Table 7 (continued)

2MASS ID	Visit	Epoch (MJD)	SDSS plate & Fiber	SNR	$v_{prim}(\frac{km}{s})$	$v_{sec}(\frac{km}{s})$
	2	56677.2508	6552-56677-250	232	102.5	44.5
	3 ²	56700.2056	6552-56700-250	245	63.09	79.31
2M07444028+7946423	1	56349.2512	6566-56349-237	213	8.6	-43.7
	2	56640.4901	6566-56640-279	232	-26.6	-14.4
	3	56650.4149	6566-56650-226	176	-66.7	24.4
2M08100405+3220142	1 ¹	56323.3399	6778-56323-213	143	7.24±0.15	30.69±0.15
	2 ¹	56349.3061	6778-56349-225	163	21.84±0.16	14.99±0.18
	3 ¹	56353.2618	6778-56353-213	167	18.79±0.22	18.56±0.23
	4 ¹	56324.3037	6779-56324-220	145	6.50±0.19	31.19±0.20
	5 ¹	56352.2445	6779-56352-220	144	18.73±0.25	18.62±0.27
	6 ¹	56372.2128	6779-56372-220	137	35.69±0.13	1.68±0.14
2M10423925+1944404	1 ¹	56264.5342	6576-56264-045	57	-4.42±0.40	-25.49±0.40
	2 ¹	56288.5058	6613-56288-052	87	-1.96±0.32	-28.09±0.32
	3 ¹	56313.3796	6613-56313-051	67	-0.56±0.47	-30.12±0.44
	4 ¹	56314.3304	6613-56314-051	72	-1.59±0.39	-29.68±0.43
2M10464238+1626144	1 ¹	55967.3129	5680-55967-015	56	-15.51±0.32	-58.44±0.47
	2 ¹	55989.2456	5680-55989-022	43	-66.65±0.26	1.45±0.43
	3 ¹	55990.2372	5680-55990-022	72	-22.06±0.24	-52.50±0.35
2M11081979+4751217	1	56675.4195	7348-56675-089	83	-30.4	31.1
	2	56698.3212	7348-56698-089	56	-	-
	3	56700.3171	7348-56700-089	66	-30.8	33.5
	4	56704.3391	7348-56704-071	8	-29.9	28.1
	5	56729.2837	7348-56729-065	69	-28.3	21.8
2M12045611+1728119	1 ¹	55968.3811	5683-55968-260	205	-46.36±0.16	95.09±0.48
	2 ¹	56022.2465	5683-56022-260	173	-19.67±0.22	53.37±0.59
	3	56379.2677	5683-56379-263	146	-3.0	41.5
2M12214070+2707510	1 ¹	55940.4279	5622-55940-237	91	-5.40±0.33	6.29±0.34
	2 ¹	55998.2603	5622-55998-238	115	-11.23±0.22	12.32±0.23
	3 ¹	56018.2352	5622-56018-274	129	11.63±0.21	-10.55±0.23
	4 ¹	56756.1755	7435-56756-273	138	-3.96±0.31	5.32±0.32
	5 ¹	56761.1460	7435-56761-279	119	-3.20±0.56	3.72±0.50
	6 ¹	56815.1664	7437-56815-274	132	22.10±0.24	-20.30±0.31
	7 ¹	56819.1401	7437-56819-279	100	20.23±0.27	-18.62±0.32
	8 ¹	56824.1421	7437-56824-279	123	17.59±0.21	-16.07±0.25
	9 ¹	56790.1321	7438-56790-238	118	16.55±0.23	-15.74±0.28
	10 ¹	56814.1431	7438-56814-274	136	22.40±0.23	-20.25±0.32
	11 ¹	56818.1447	7438-56818-274	132	20.75±0.19	-19.17±0.24
2M12260547+2644385	1 ¹	55940.4279	5622-55940-255	285	6.94±0.35	-8.34±0.12
	2 ¹	55998.2603	5622-55998-291	349	11.85±0.12	-13.72±0.33
	3 ¹	56018.2352	5622-56018-160	467	11.00±0.12	-14.29±0.30
	4 ¹	56756.1755	7435-56756-154	436	8.99±0.48	-9.06±0.16
	5 ¹	56761.1460	7435-56761-195	393	6.96±0.45	-10.20±0.14
	6 ¹	56815.1664	7437-56815-245	422	-16.14±0.17	22.71±0.37
	7 ¹	56819.1401	7437-56819-206	340	-14.77±0.20	20.49±0.42
	8 ¹	56824.1421	7437-56824-290	393	-12.06±0.12	15.93±0.28
	9 ¹	56790.1321	7438-56790-195	370	-17.14±0.12	22.87±0.30
	10 ¹	56814.1431	7438-56814-208	454	-16.86±0.17	23.68±0.34
	11 ¹	56818.1447	7438-56818-201	477	-15.20±0.13	20.70±0.27
2M12260848+2439315	1	56756.1755	7435-56756-143	66	-19.1	22.3
	2	56761.1460	7435-56761-131	62	18.7	-12.5

Table 7 continued

Table 7 (continued)

2MASS ID	Visit	Epoch (MJD)	SDSS plate & Fiber	SNR	$v_{prim}(\frac{km}{s})$	$v_{sec}(\frac{km}{s})$
	3	56815.1664	7437-56815-134	65	-18.2	23.2
	4	56819.1401	7437-56819-137	43	-14.5	21.5
	5	56824.1421	7437-56824-131	62	1.8	1.8
	6	56790.1321	7438-56790-137	55	-13.3	19.8
	7	56814.1431	7438-56814-146	65	-18.1	23.3
	8	56818.1447	7438-56818-131	73	-16.2	23.2
2M14545496+4108480	1	56378.3525	6852-56378-022	151	41.8	-38.6
	2	56405.3445	6852-56405-010	123	-22.4	32.9
	3	56409.3016	6852-56409-003	114	50.4	-49.0
	4	56411.3084	6852-56411-022	152	-19.0	29.8
2M14551346+4128494	1	56378.3525	6852-56378-230	79	-55.0	44.4
	2	56405.3445	6852-56405-218	74	-31.9	15.6
	3	56409.3016	6852-56409-218	71	30.8	-68.6
	4	56411.3084	6852-56411-221	93	26.6	-66.7
2M14562809+1648342	1	56432.2611	6844-56432-045	262	14.5	32.0
	2	56470.1510	6844-56470-033	279	16.8	2.7
	3	56703.4974	6844-56703-135	354	-8.2	45.7
2M17204248+4205070	1 ¹	55992.4532	5670-55992-130	166	36.59±0.30	-72.86±0.61
	2 ¹	55998.4958	5671-55998-129	183	11.76±0.37	-34.88±0.66
	3 ¹	55999.4819	5670-55999-076	225	25.74±0.36	-56.06±0.89
	4 ¹	56019.3882	5670-56019-076	105	12.33±0.52	-36.15±0.91
	5 ¹	56022.4230	5670-56022-075	204	28.85±0.33	-60.66±0.84
	6 ¹	56023.4295	5670-56023-075	198	-43.60±0.33	49.59±0.68
	7 ¹	56025.4247	5671-56025-135	171	36.49±0.56	-72.81±1.79
	8 ¹	56027.4338	5671-56048-129	164	-38.12±0.32	40.81±0.88
	9 ¹	56048.3635	5671-56049-129	184	37.18±0.30	-73.09±0.63
	10 ¹	56049.3599	5837-56027-076	199	-19.13±0.30	14.02±0.77
	11 ¹	56054.3636	5838-56054-130	129	11.04±0.43	-32.74±0.82
	12 ¹	56084.2389	5838-56084-088	201	30.01±0.32	-62.89±0.80
	13 [*]	56429.2314	-	88	24.82±0.16	-54.70±0.22
	14 [*]	56434.2142	-	72	-41.71±0.16	45.62±0.21
	15 [*]	56439.2273	-	84	31.73±0.16	-65.23±0.20
	16 [*]	56444.2160	-	94	-47.27±0.16	54.96±0.18
	17 [*]	56472.3738	-	76	37.20±0.16	-73.06±0.20
	18 ¹	56052.4257	5837-56052-129	176	-1.55±0.52	-13.58±1.07
	19	56351.5046	5837-56351-076	176	-5.2	-
	20	56362.5225	5838-56362-130	139	-44.4	53.0
2M19081153+2839105	1	56082.4258	5246-56082-274	144	33.1	-
	2	56086.4331	5246-56086-274	167	37.4	16.8
	3	56091.4578	5246-56091-279	95	38.1	17.3
	4	56084.4143	5247-56084-236	149	38.2	17.7
	5	56088.4135	5247-56088-281	133	33.0	-
	6	56092.4589	5247-56092-281	87	33.2	-
	7	56093.4469	5247-56093-281	121	37.4	16.7
	8	56779.3534	7475-56779-220	129	36.8	18.4
	9	56825.2622	7475-56825-273	111	23.3	33.7
	10	56831.3617	7476-56831-273	134	5.6	53.3
	11	56775.3457	7477-56775-274	81	28.4	-
	12	56781.3197	7477-56781-273	119	37.2	18.7
	13	56799.3399	7477-56799-280	131	37.7	16.4

Table 7 continued

Table 7 (continued)

2MASS ID	Visit	Epoch (MJD)	SDSS plate & Fiber	SNR	$v_{prim}(\frac{km}{s})$	$v_{sec}(\frac{km}{s})$
2M19235494+3834587	1 ¹	55811.1100	5213-55811-283	41	-52.70±0.47	12.32±0.49
	2 ¹	55840.0915	5213-55840-241	50	1.68±0.38	-41.62±0.40
	3 ¹	55851.0793	5213-55851-283	58	-1.49±0.34	-38.29±0.36
	4*	56429.3213	-	35	-38.99±0.20	0.00±0.23
	5*	56434.3099	-	34	40.99±0.28	-83.73±0.21
	6*	56439.3063	-	33	-89.67±0.28	46.22±0.28
	7*	56444.2909	-	45	-27.41±0.22	-10.09±0.20
	8*	56450.2800	-	35	-100.80±0.22	60.46±0.19
	9*	56472.2149	-	38	-50.90±0.22	12.27±0.20
2M19433790+3225124	1	56603.0524	6079-56603-184	485	-19.1	-
	2	56749.4836	7463-56749-231	470	-18.5	-24.5
	3	56754.4648	7463-56754-183	549	5.4	-53.3
2M20474087+3343054	1	56604.0570	6081-56604-160	247	-46.7	15.5
	2	56611.0588	6081-56611-261	280	19.5	-57.5
	3	56808.3481	7465-56808-159	236	-18.3	-18.5
2M21005978+5103147	1	56623.0461	6949-56623-166	176	-48.5	-60.4
	2	56809.4544	6949-56809-165	127	-83.5	-26.4
	3	56626.0540	6950-56626-166	215	-26.3	-83.5
	4	56817.4235	7491-56817-165	206	-68.9	-40.3
	5	56836.4321	7493-56836-165	235	-32.6	-78.3
2M21234344+4419277	1	56261.0499	6085-56261-117	83	-164.5	-77.8
	2	56479.4540	6085-56479-118	46	-163.9	-77.8
	3	56263.0643	6086-56263-117	85	-86.6	-162.2
	4	56485.4644	6086-56485-117	6	-77.6	-178.0
	5	56486.4616	6086-56486-117	30	-105.8	-141.5
	6	56589.1833	6086-56589-105	11	-107.5	-143.7
	7	56599.1220	6086-56599-105	45	-65.2	-186.3
	8	56603.1091	6086-56603-105	71	-183.3	-59.0
2M21442066+4211363	1	55870.1160	5254-55870-046	59	-70.6	53.6
	2	56170.2919	5254-56170-040	65	-79.1	44.1
	3	56193.2333	5254-56193-046	80	-79.3	45.0
	4	55869.1221	5255-55869-051	89	3.7	-27.7
	5	56171.2829	5255-56171-087	79	10.1	-47.9
	6	56204.1936	5255-56204-045	61	4.0	-40.3
	7	56205.2364	6248-56205-089	103	26.5	-67.7
	8	56221.2010	6248-56221-035	112	40.4	-80.7
	9	56231.1930	6248-56231-035	82	44.2	-80.1
	10	56206.2158	6249-56206-034	89	-73.4	35.9
	11	56223.1801	6249-56223-034	87	-76.6	41.6
	12	56232.1857	6249-56232-033	68	-34.1	-0.6

NOTE—Dashed out velocities indicate spurious RVs omitted from analysis. RVs not extracted via TODCOR are assigned the ensemble uncertainty of $\sim 1.8 \frac{km}{s}$.

* These visits are from the Hobby-Eberly Telescope (HET) High-Resolution Spectrograph (HRS). SNR is highly wavelength dependent for M-dwarfs; values reported here are at 7500 nm. TODCOR was used for RV extraction.

¹ TODCOR used for RV extraction.

² Radial velocities for these epochs were mis-assigned by the extraction routine described in section §3.1, and manually corrected.

REFERENCES

- Abrams, M. C., Davis, S. P., Rao, M. L. P., Engleman, Jr., Albareti, F. D. et al. 2017, ApJS, 233, 25
 R., & Brault, J. W. 1994, ApJS, 93, 351

- Allard, F., Homeier, D., Freytag, B., & Sharp, C. M. 2012, in *EAS Publications Series*, Vol. 57, *EAS Publications Series*, ed. C. Reylé, C. Charbonnel, & M. Schultheis, 3–43
- Bate, M. R., Bonnell, I. A., & Bromm, V. 2002, *MNRAS*, 336, 705
- Bender, C., Simon, M., Prato, L., Mazeh, T., & Zucker, S. 2005, *AJ*, 129, 402
- Bender, C. F. et al. 2012, *ApJL*, 751, L31
- Burgasser, A. J., Kirkpatrick, J. D., Cruz, K. L., Reid, I. N., Leggett, S. K., Liebert, J., Burrows, A., & Brown, M. E. 2006, *ApJS*, 166, 585
- Ciardi, D. R. et al. 2011, *AJ*, 141, 108
- Claret, A. 2000, *A&A*, 363, 1081
- Clark, B. M., Blake, C. H., & Knapp, G. R. 2012, *ApJ*, 744, 119
- Clough, S. A., Shephard, M. W., Mlawer, E. J., Delamere, J. S., Iacono, M. J., Cady-Pereira, K., Boukabara, S., & Brown, P. D. 2005, *JQSRT*, 91, 233
- Cushing, M. C., Vacca, W. D., & Rayner, J. T. 2004, *PASP*, 116, 362
- Delfosse, X., Forveille, T., Ségransan, D., Beuzit, J.-L., Udry, S., Perrier, C., & Mayor, M. 2000, *A&A*, 364, 217
- Deshpande, R. et al. 2013, *AJ*, 146, 156
- Duchêne, G., & Kraus, A. 2013, *ARA&A*, 51, 269
- Eisenstein, D. J. et al. 2011, *AJ*, 142, 72
- El-Badry, K., Rix, H.-W., Ting, Y.-S., Weisz, D. R., Bergemann, M., Cargile, P., Conroy, C., & Eilers, A.-C. 2018a, *MNRAS*, 473, 5043
- El-Badry, K. et al. 2018b, *MNRAS*, 476, 528
- Fabrycky, D., & Tremaine, S. 2007, *ApJ*, 669, 1298
- Fernandez, M. A. et al. 2017, *PASP*, 129, 084201
- Fischer, D. A., & Marcy, G. W. 1992, *ApJ*, 396, 178
- Foreman-Mackey, D., Hogg, D. W., Lang, D., & Goodman, J. 2013, *PASP*, 125, 306
- García Pérez, A. E. et al. 2016, *AJ*, 151, 144
- Gilhool, S. H., Blake, C. H., Terrien, R. C., Bender, C., Mahadevan, S., & Deshpande, R. 2018, *AJ*, 155, 38
- Goodman, Jonathan; Weare, J. 2010, *Communications in Applied Mathematics and Computational Science*, 5
- Gorti, U., & Bhatt, H. C. 1996, *MNRAS*, 283, 566
- Grievés, N. et al. 2017, *MNRAS*, 467, 4264
- Gunn, J. E. et al. 2006, *AJ*, 131, 2332
- Holtzman, J. A. et al. 2015, *AJ*, 150, 148
- Jenkins, J. S., Ramsey, L. W., Jones, H. R. A., Pavlenko, Y., Gallardo, J., Barnes, J. R., & Pinfield, D. J. 2009, *ApJ*, 704, 975
- Kiseleva, L. G., Eggleton, P. P., & Mikkola, S. 1998, *MNRAS*, 300, 292
- Kratter, K. M. 2011, in *Astronomical Society of the Pacific Conference Series*, Vol. 447, *Evolution of Compact Binaries*, ed. L. Schmidtbreick, M. R. Schreiber, & C. Tappert, 47
- Kraus, A. L., & Hillenbrand, L. A. 2007, *AJ*, 134, 2340
- Lépine, S., & Gaidos, E. 2011, *AJ*, 142, 138
- Lépine, S., & Shara, M. M. 2005, *AJ*, 129, 1483
- Majewski, S. R. et al. 2017, *AJ*, 154, 94
- Mann, A. W., Feiden, G. A., Gaidos, E., Boyajian, T., & von Braun, K. 2015, *ApJ*, 804, 64
- Moe, M., & Di Stefano, R. 2017, *ApJS*, 230, 15
- Murphy, M. T., Tzanavaris, P., Webb, J. K., & Lovis, C. 2007, *MNRAS*, 378, 221
- Nidever, D. L. et al. 2015, *AJ*, 150, 173
- Nutzman, P., & Charbonneau, D. 2008, *PASP*, 120, 317
- Offner, S. S. R., Kratter, K. M., Matzner, C. D., Krumholz, M. R., & Klein, R. I. 2010, *ApJ*, 725, 1485
- Pourbaix, D. et al. 2004, *A&A*, 424, 727
- Qi, Z. et al. 2015, *AJ*, 150, 137
- Raghavan, D. et al. 2010, *ApJS*, 190, 1
- Ramsey, L. W. et al. 1998, in *Proc. SPIE*, Vol. 3352, *Advanced Technology Optical/IR Telescopes VI*, ed. L. M. Stepp, 34–42
- Reipurth, B., & Clarke, C. 2001, *AJ*, 122, 432
- Shan, Y., Johnson, J. A., & Morton, T. D. 2015, *ApJ*, 813, 75
- Shetrone, M. et al. 2007, *PASP*, 119, 556
- Souto, D. et al. 2017, *ApJ*, 835, 239
- Tohline, J. E. 2002, *ARA&A*, 40, 349
- Tonry, J., & Davis, M. 1979, *AJ*, 84, 1511
- Tull, R. G. 1998, in *Proc. SPIE*, Vol. 3355, *Optical Astronomical Instrumentation*, ed. S. D’Odorico, 387–398
- Viaux, N., Catelan, M., Stetson, P., Raffelt, G., Redondo, J., Valcarce, A., & Weiss, A. 2013, *VizieR Online Data Catalog*, 355
- Walkowicz, L. M. et al. 2011, *AJ*, 141, 50
- Ward-Duong, K. et al. 2015, *MNRAS*, 449, 2618
- Wilson, J. C. et al. 2010, in *Proc. SPIE*, Vol. 7735, *Ground-based and Airborne Instrumentation for Astronomy III*, 77351C
- Wilson, J. C. et al. 2012, in *Proc. SPIE*, Vol. 8446, *Ground-based and Airborne Instrumentation for Astronomy IV*, 84460H
- Wilson, O. C. 1941, *ApJ*, 93, 29
- Zacharias, N., Finch, C., & Frouard, J. 2017, *AJ*, 153, 166
- Zacharias, N., Finch, C. T., Girard, T. M., Henden, A., Bartlett, J. L., Monet, D. G., & Zacharias, M. I. 2013, *AJ*, 145, 44

Zacharias, N., Monet, D. G., Levine, S. E., Urban, S. E.,
Gaume, R., & Wycoff, G. L. 2005, VizieR Online Data
Catalog, 1297

Zasowski, G. et al. 2013, AJ, 146, 81

Zucker, S., & Mazeh, T. 1994, ApJ, 420, 806

Zucker, S., Torres, G., & Mazeh, T. 1995, ApJ, 452, 863